nature catalysis

Article

https://doi.org/10.1038/s41929-023-01091-3

Acid-stable manganese oxides for proton exchange membrane water electrolysis

In the format provided by the authors and unedited

Table of Contents (section titles correspond to those in the main text)

Supplementary Figures

Catalyst Characterization

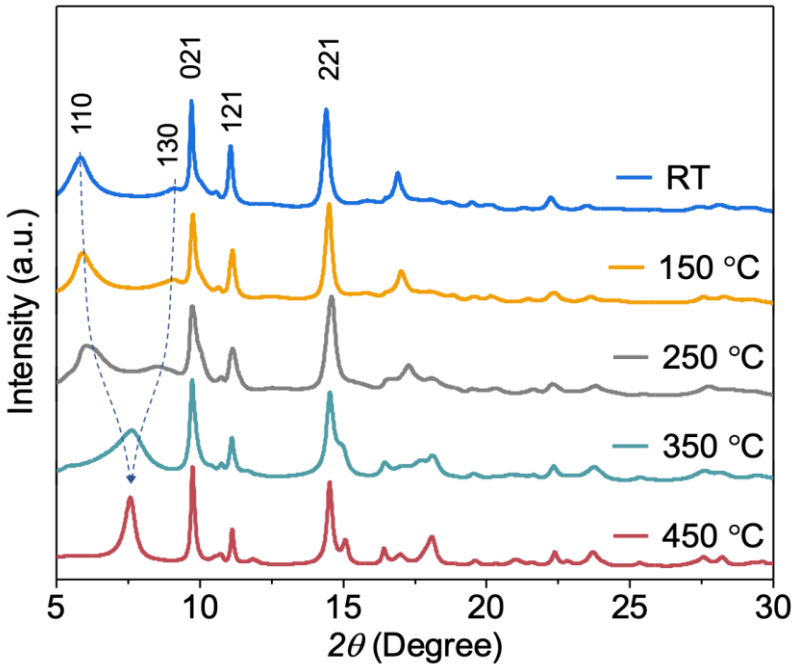

Supplementary Figure 1. Synchrotron radiation powder X-ray diffraction of γ-MnO_2 samples.
The synchrotron radiation powder X-ray diffraction (SR-PXRD) patterns of the synthesized γ-MnO_2 samples. The merging of the 110 and 130 peaks from M60% to M94% indicates the conversion of ramsdellite to pyrolusite upon increasing the annealing temperature from 150 to 450 °C[1]. The sample without annealing (RT) is given for comparison.

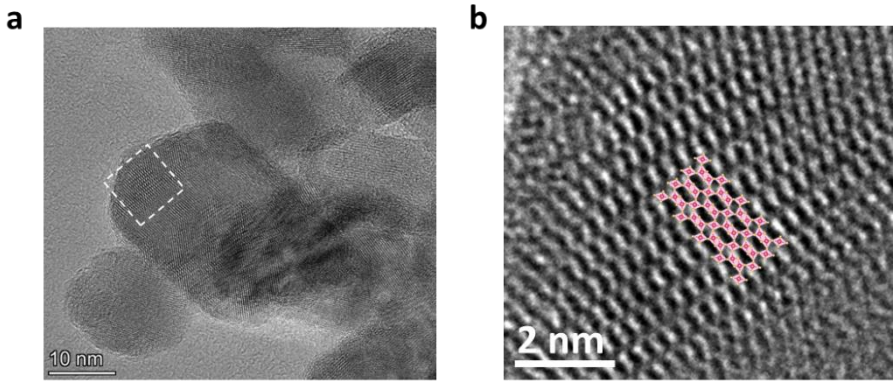

c

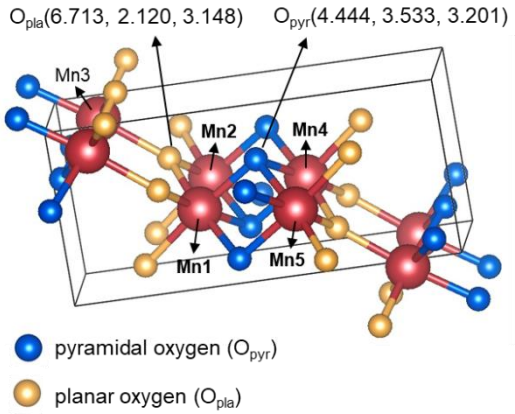

a / Å	4.385(2)
b / Å	9.495(5)
c / Å	2.826(2)
Mn	*x* = 0.006(1) *y*=0.131(4) z = 1/4
O_{pla}	*x* = 0.282(2) *y* = 0.293(1) z = 1/4
O_{pyr}	*x* = 0.730(2) *y* = 0.468(1) *z* = 1/4

Supplementary Figure 2. Structure determination from HRTEM images and PDF refinement.

(**a**) High-resolution transmission electron microscopy (HRTEM) images of M94%, with a scale bar of 10 nm. (**b**) An enlarged image showing the lattice-resolved TEM image of M94% within the rectangle shown in (**a**), with a scale bar of 2 nm. The schematic diagram comparing the crystal structure of γ-MnO_2 (cif: CSD 1514239)[2] is shown, with an intergrowth of both single and double [MnO_6] unit cells. (**c**) The planar oxygen (O_{pla}) and pyramidal oxygen (O_{pyr}) were identified from the PDF analysis. The table displays the fitted structural parameters of R-MnO_2 blocks within M64%, obtained from PDF refinement. The yellow spheres represent the O_{pla} and the blue spheres represent the O_{pyr}.

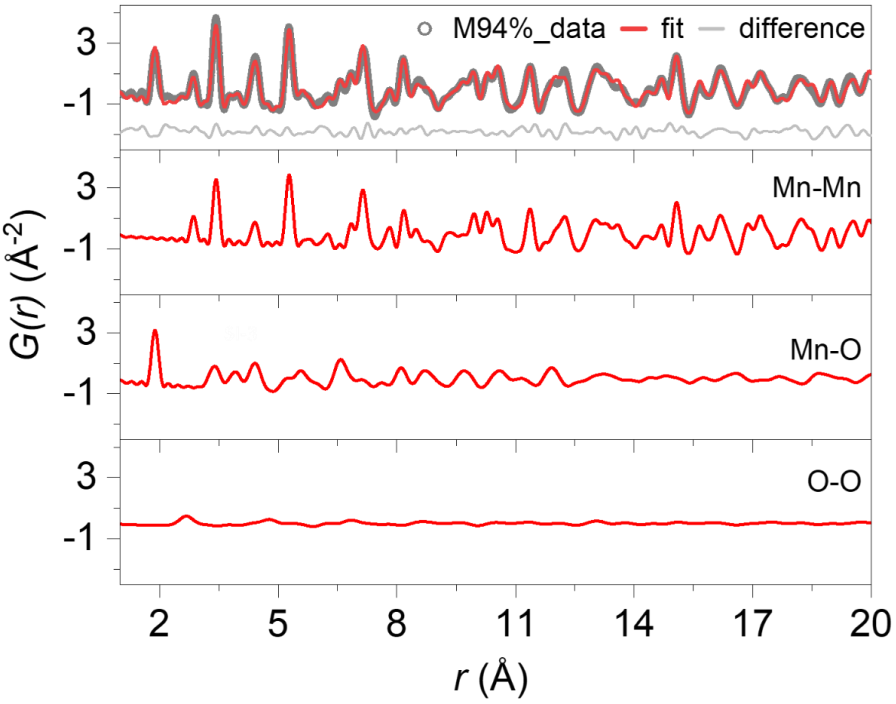

Supplementary Figure 3. Pair distribution function of M94%.
Refinement of the pair distribution function (PDF) of M94%, as well as the decomposition of the fitted PDF into contributions from the Mn-Mn (Mn-Mn partial PDF), Mn-O (Mn-O partial PDF), and O-O (O-O partial PDF) atom pairs. The fitted parameters are provided in Supplementary Table 1.

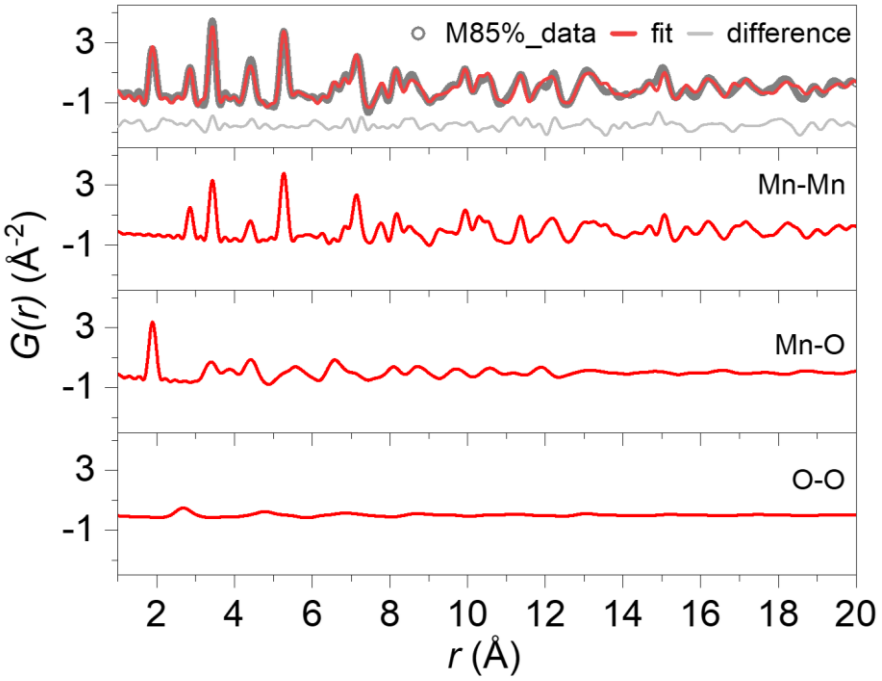

Supplementary Figure 4. Pair distribution function of M85%.
Refinement of the pair distribution function (PDF) of M85%, as well as the decomposition of the fitted PDF into contributions from the Mn-Mn (Mn-Mn partial PDF), Mn-O (Mn-O partial PDF), and O-O (O-O partial PDF) atom pairs. The fitted parameters are provided in Supplementary Table 1.

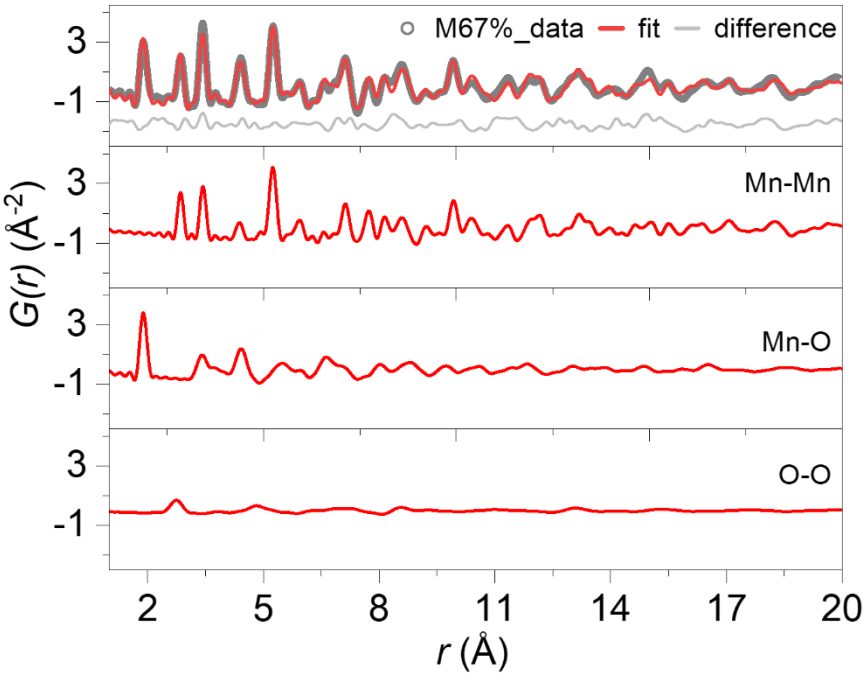

Supplementary Figure 5. Pair distribution function of M67%.
Refinement of the pair distribution function (PDF) of M67%, as well as the decomposition of the fitted PDF into contributions from the Mn-Mn (Mn-Mn partial PDF), Mn-O (Mn-O partial PDF), and O-O (O-O partial PDF) atom pairs. The fitted parameters are provided in Supplementary Table 1.

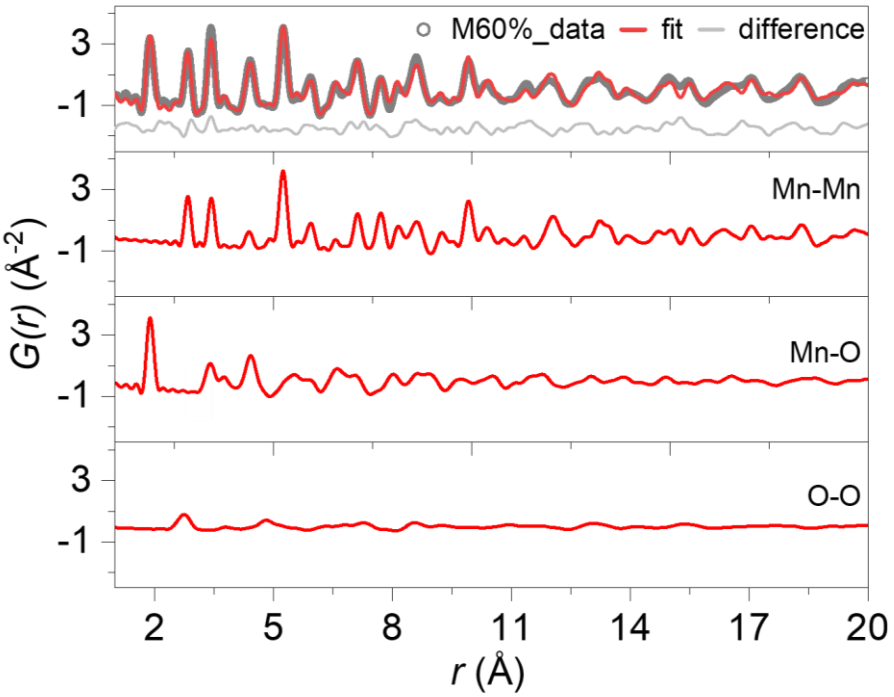

Supplementary Figure 6. Pair distribution function of M60%.
Refinement of the pair distribution function (PDF) of M60%, as well as the decomposition of the fitted PDF into contributions from the Mn-Mn (Mn-Mn partial PDF), Mn-O (Mn-O partial PDF), and O-O (O-O partial PDF) atom pairs. The fitted parameters are provided in Supplementary Table 1.

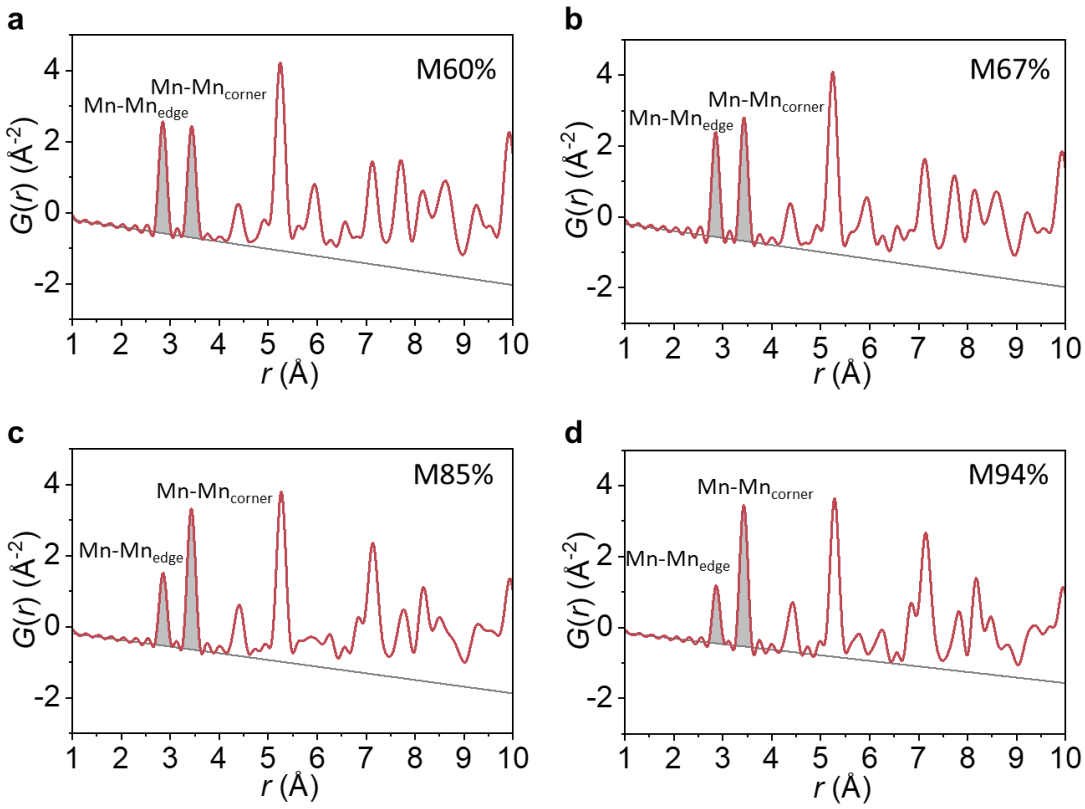

Supplementary Figure 7. Mn-Mn partial PDFs of γ-MnO_2 samples.
Mn-Mn partial PDFs of four γ-MnO_2 samples with O_{pla} concentrations of (**a**) 60%, (**b**) 67%, (**c**) 85% and (**d**) 94%. The shaded area indicates the integration of the Mn-Mn_{edge} and Mn-Mn_{corner} peaks. The grey lines indicate baselines that are based on the definition of $G(r)$, $G(r) = 4\pi\rho_0 r(g(r)-1)$. As $r \rightarrow +0$, this function behaves like $-4\pi\rho_0 r$ and passes through zero with a slope that is proportional to the average number density (ρ_0) of the material. The percentage of Mn-Mn_{corner} was calculated as $A_1 \times r_1/(A_1 \times r_1 + A_2 \times r_2)$, where A_1 and A_2 are the integrated peak area of Mn-Mn_{corner} and Mn-Mn_{edge}, and r_1 and r_2 are the corresponding peak positions[3,4].

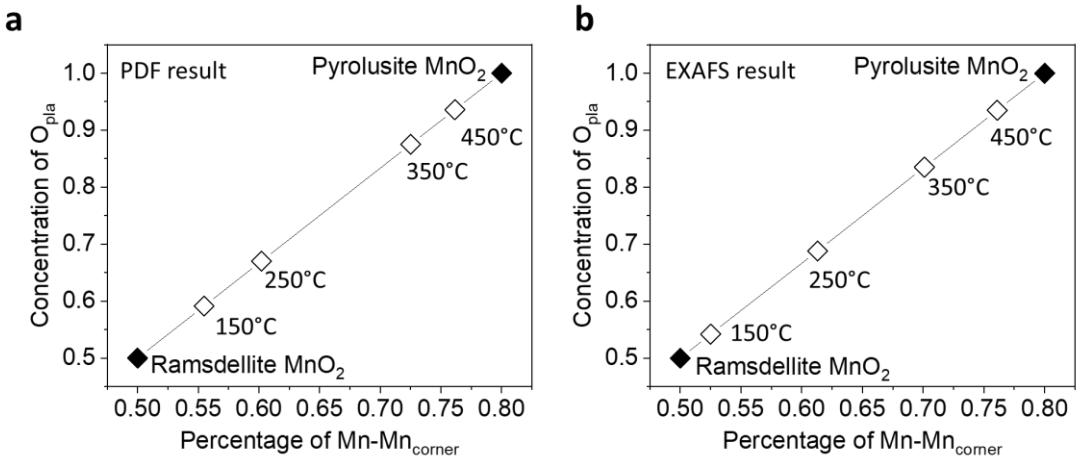

c

	M60%	M67%	M85%	M94%
Mn-Mn_{corner} (PDF)	56.2%	60.3%	70.8%	76.2%
Mn-Mn_{corner} (EXAFS)	52.5%	61.3%	70.1%	76.1%
O_{pla} (PDF)	60.3%	67.2%	84.7%	93.7%
O_{pla} (EXAFS)	54.2%	68.8%	83.5%	93.5%

Supplementary Figure 8. Quantitative analysis based on PDF and EXAFS. Calculation of O_{pla} based on the linear relationship between O_{pla} and Mn-Mn_{corner} obtained from the PDF (**a**) and EXAFS analysis (**b**). The void points represent the four γ-MnO_2 samples annealed at 150, 250, 350, and 450 °C. The solid points represent pure ramsdellite and pure pyrolusite MnO_2. Pure ramsdellite MnO_2 has 50% Mn-Mn_{corner}, which corresponds to 50% O_{pla}[5]. Pure pyrolusite MnO_2 has 80% Mn-Mn_{corner}, which corresponds to 100% O_{pla}[5]. As γ-MnO_2 is an intergrowth of ramsdellite and pyrolusite MnO_2, the concentration of O_{pla} in γ-MnO_2 displays a linear change with Mn-Mn_{corner}. The deviation of the O_{pla} concentration derived from PDF and EXAFS analysis is less than 6%. (**c**) Table shows the numerical values of Mn-Mn_{corner} ratio and the concentration of O_{pla} obtained from the PDF and EXAFS analysis, respectively.

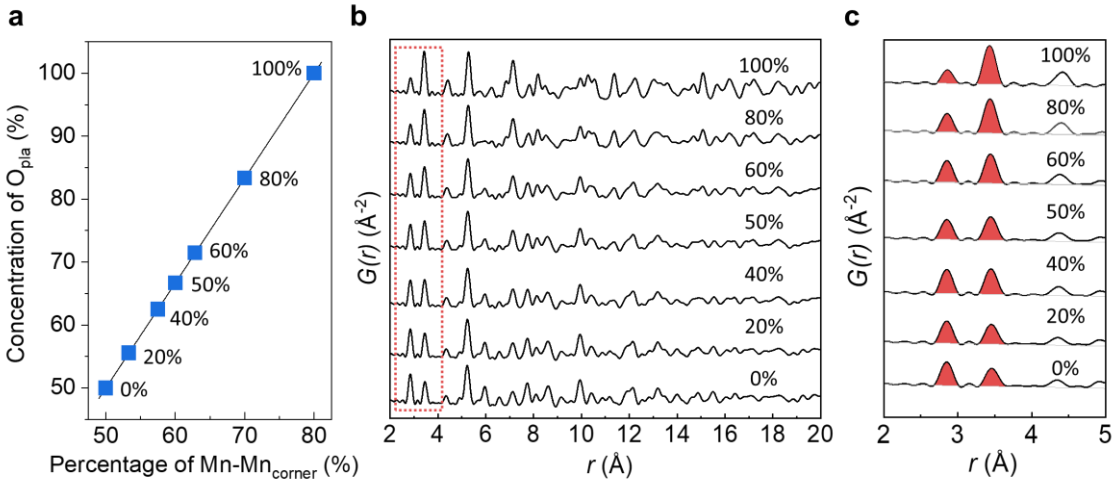

d

β-MnO_2 percentage	A1	r1	A2	r2	Fitted Mn-Mn_{Corner} ratio	Fitted O_{pla} ratio	Theoretical Mn-Mn_{Corner} ratio	Theoretical O_{pla} ratio	Error of O_{pla}
100%	2.285	3.430	0.688	2.861	79.9%	99.9%	80.0%	100.0%	0.1%
80%	1.900	3.436	0.937	2.856	70.9%	84.9%	70.0%	83.3%	1.6%
60%	1.630	3.442	1.117	2.854	63.7%	72.9%	62.9%	71.4%	1.4%
50%	1.580	3.445	1.231	2.853	60.8%	68.0%	60.0%	66.7%	1.3%
40%	1.403	3.448	1.233	2.852	58.2%	63.6%	57.5%	62.5%	1.1%
20%	1.337	3.454	1.401	2.851	53.6%	56.1%	53.3%	55.6%	0.5%
0%	1.218	3.459	1.485	2.850	49.9%	49.8%	50.0%	50.0%	0.2%

Supplementary Figure 9. Analysis accuracy of PDF refinement.
(a) The theoretical concentration of O_{pla} plotted versus the theoretical Mn-Mn_{corner} ratio in γ-MnO_2 with β-MnO_2 percentages of 80%, 60%, 50%, 40%, and 20%. 100% and 0% correspond to β-MnO_2 and R-MnO_2, respectively. **(b)** Simulated Mn-Mn partial PDF patterns of β-MnO_2, R-MnO_2, and γ-MnO_2 with β-MnO_2 percentages of 80%, 60%, 50%, 40%, and 20%, respectively. (**c**) The integration of Mn-Mn_{edge} and Mn-Mn_{corner} peaks (shaded area). The ratio of Mn-Mn_{corner} was calculated by $A_1 \times r_1/(A_1 \times r_1 + A_2 \times r_2)$, where A_1 and A_2 are the integrated peak area of Mn-Mn_{corner} and Mn-Mn_{edge}, and r_1 and r_2 are the corresponding peak positions. (**d**) Theoretical and fitted parameters of β-MnO_2, R-MnO_2, and γ-MnO_2 with β-MnO_2 percentages of 80%, 60%, 50%, 40%, and 20%, respectively. The comparison between the fitted result with their theoretical O_{pla} concentration indicates an error of within 2%.

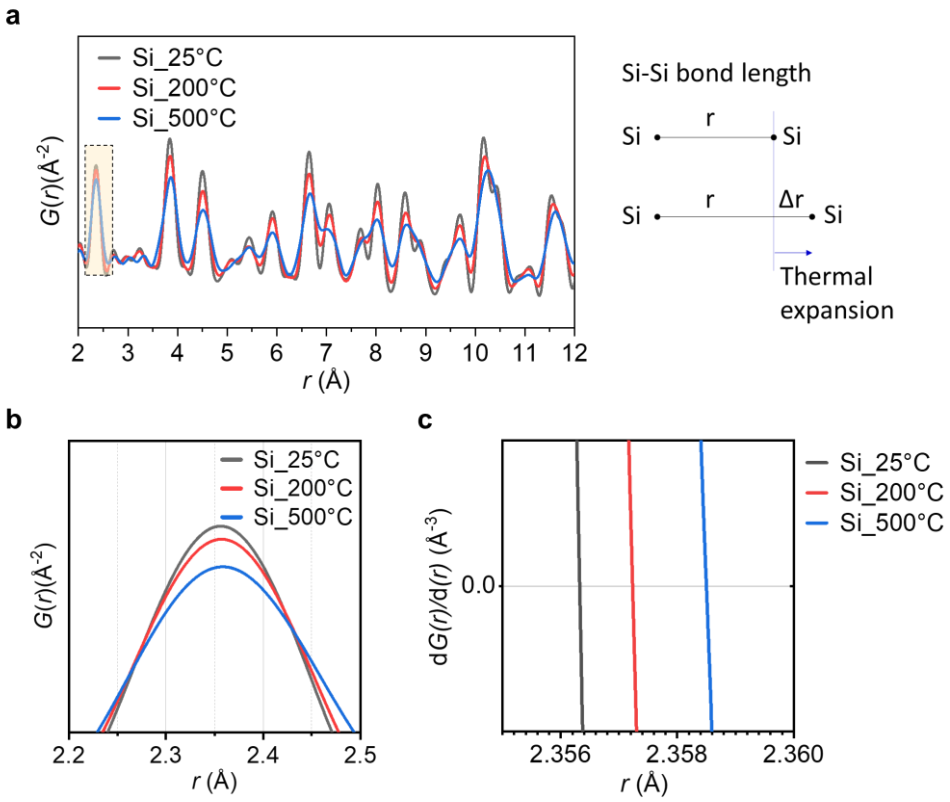

Supplementary Figure 10. Pair distribution function analysis of Si.
(**a**) Pair distribution function analysis of Si standard samples (Silicon Powder X-ray diffraction standard, NIST SRM 640) measured at 25, 200, and 500 °C, respectively. The first Si-Si peak (**b**) and its peak derivative (**c**) indicate an expansion in Si-Si bond length at 200, and 500 °C compared to that of 25 °C.

The Si-Si bond expansion was observed to be 0.0009 and 0.0022 Å at 200 and 500°C compared to that at 25°C. This result is consistent well with the theoretical values of approximately 0.0010 and 0.0029 Å at 200 and 500°C[6], respectively. It revealed that PDF experiments are capable of detecting bond length changes as small as 0.001 Å, confirming the high experimental accuracy of PDF.

a

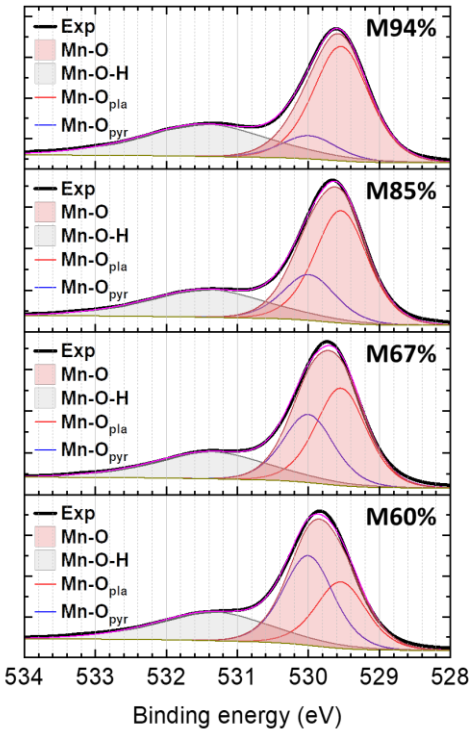

b

Sample	Name	Position (eV)	Name	Position (eV)	Name	Position (eV)	$O_{pla}/(O_{pla}+O_{pyr})$ ratio (%)
M60%	Lattice oxygen	529.80	Metal hydroxide	531.42	O_{pla} O_{pry}	529.51 529.96	42.4%
M67%	Lattice oxygen	529.69	Metal hydroxide	531.42	O_{pla} O_{pry}	529.51 529.96	61.2%
M85%	Lattice oxygen	529.62	Metal hydroxide	531.44	O_{pla} O_{pry}	529.51 529.96	74.7%
M94%	Lattice oxygen	529.56	Metal hydroxide	531.43	O_{pla} O_{pry}	529.51 529.96	85.9%

Supplementary Figure 11. O1s XPS spectra of γ-MnO_2 samples.
(**a**) O*1s* XPS spectra of M60%, M67%, M85%, and M94%. The main peaks observed at 529.5-530 eV are attributed to lattice oxygen, whereas the shoulder peaks at 531.4 eV are attributed to the terminal hydrated oxygen[7]. The Gaussian-Lorentzian line shape GL(60) is used for the XPS analysis. The full width at half maximum (FWHM) values are 0.87 eV, 0.87 eV, and 2.10 eV for O_{pla}, O_{pyr}, and hydroxide, respectively. The quantitative analysis was performed by fitting the XPS data using a binding energy of 529.51 eV for O_{pla} and 529.96 eV for O_{pyr}, based on the binding energy of planar oxygen in β-MnO_2 and pyramidal oxygen in manganite γ-MnOOH[7], respectively. (**b**) Table summarized the fitting parameters of XPS analysis. The spectra were obtained using a pass energy of 23.5 eV and calibrated using the C1s peak at 284.6 eV.

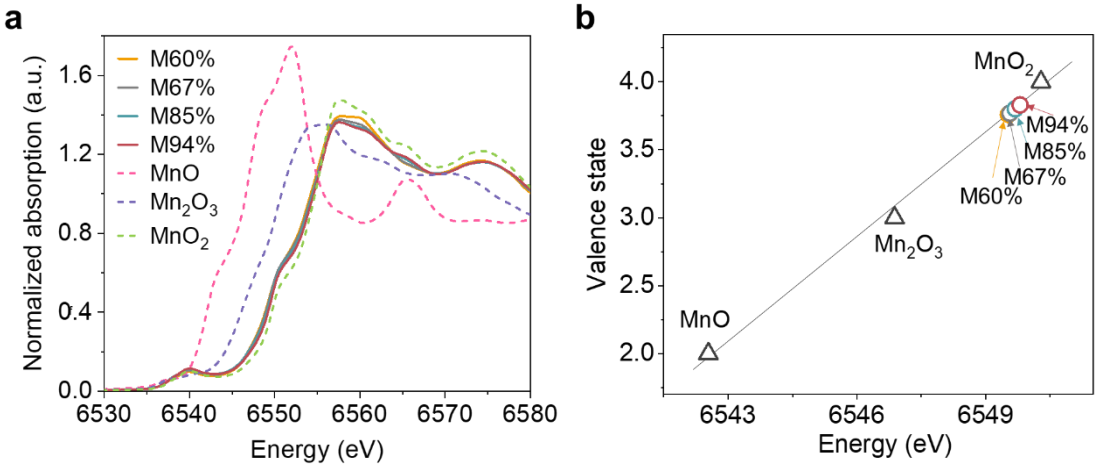

Supplementary Figure 12. Mn K-edge XANES spectra of γ-MnO_2 samples. (**a**) Mn K-edge X-ray absorption near edge structure (XANES) spectra of M60%, M67%, M85%, and M94%. (**b**) Edge position (defined as the energy at which the normalized absorption is 0.5) plotted against the Mn oxidation state. MnO, Mn_2O_3, and MnO_2 with known Mn valences were characterized as reference samples.

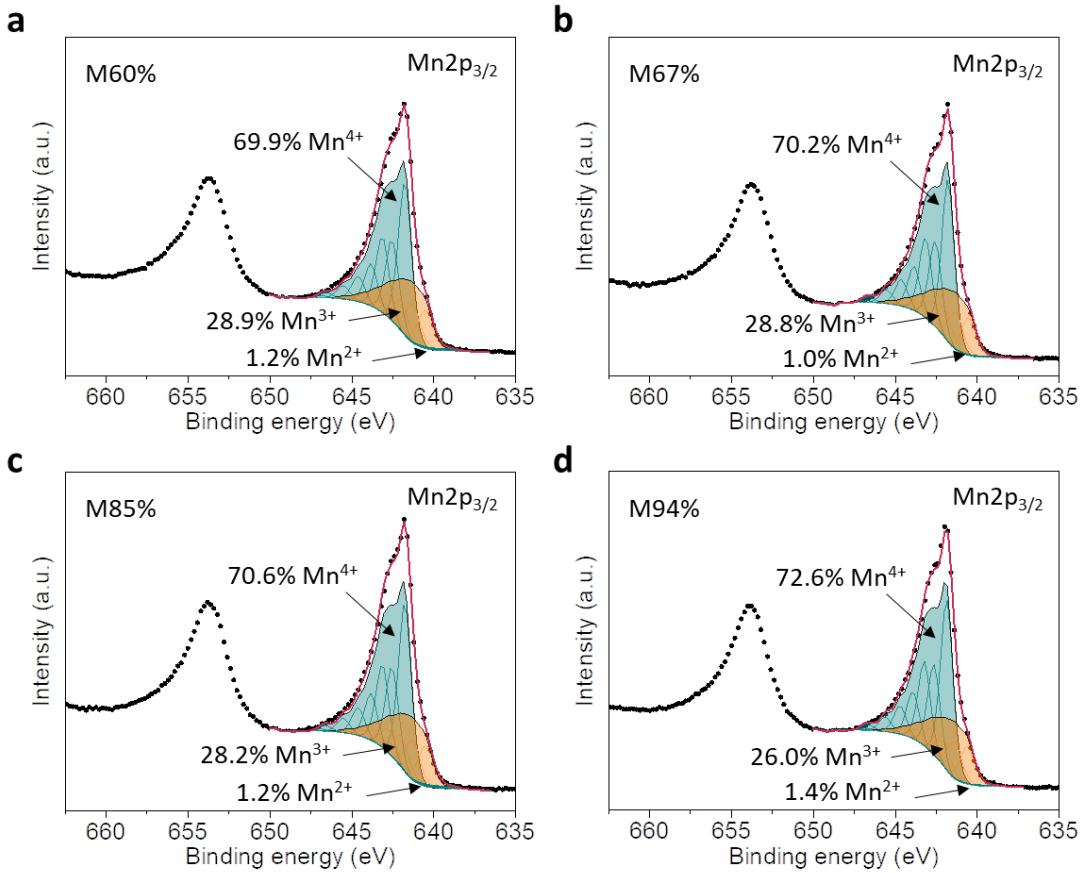

Supplementary Figure 13. Mn2p XPS spectra of γ-MnO_2 samples.
XPS spectra of Mn2p in γ-MnO_2 catalyst: (a) M60%, (b) M67%, (c) M85%, and (d) M94%. The fitting parameters of the $Mn2p_{3/2}$ spectra[8], such as the relative amounts of each oxidation state, were presented in Supplementary Table 7. The spectra were obtained using a pass energy of 23.5 eV and calibrated using the C1s peak at 284.6 eV.

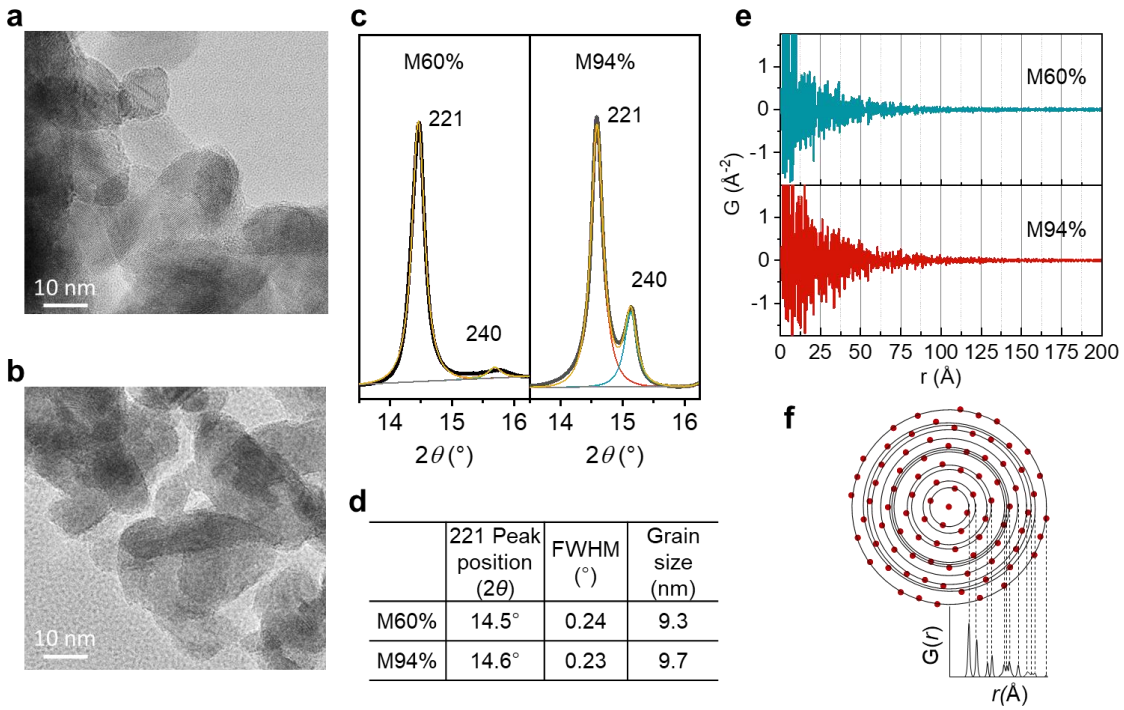

d

	221 Peak position (2θ)	FWHM (°)	Grain size (nm)
M60%	14.5°	0.24	9.3
M94%	14.6°	0.23	9.7

Supplementary Figure 14. Particle size analysis of γ-MnO_2 samples.
HR-TEM images of M60% (**a**) and M94% (**b**). Scale bar, 10 nm. (**c**) The synchrotron radiation powder X-ray diffraction (SR-PXRD) patterns of M60% and M94% exhibit 221 and 240 diffraction peaks. (**d**) The average grain sizes of M60% and M94% were estimated based on the Scherrer Equation[9]. (**e**) The pair distribution function (PDF) of M60% and M94%. (**f**) The schematic diagram depicts the average distribution of interatomic distances and numbers in a hypothetical square lattice of atoms (represented as points). The distribution shows peaks at distances between pairs of atoms, with the area of each peak proportional to the number of atoms at that distance[10]. The decay position of *G*(r) curves provides the average grain size of analyzed samples.

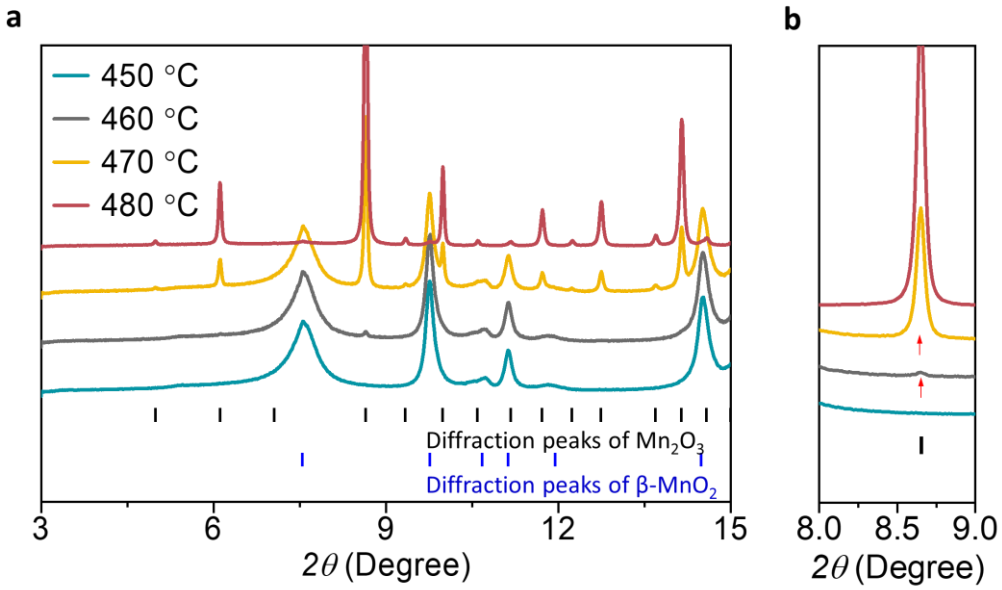

Supplementary Figure 15. Synchrotron radiation powder X-ray diffraction of Mn_2O_3.
(a) The synchrotron radiation powder X-ray diffraction (SR-PXRD) patterns of the samples annealed between 450 and 480 °C. Even at 460 °C, Mn_2O_3 was detected indicating that γ-MnO_2 is decomposed at temperature above 460 °C. The area between 8.0° and 9.0° was enlarged in (**b**). The feature peak of Mn_2O_3 at 8.6° can be clearly observed even when the sample was annealed at 460 °C.

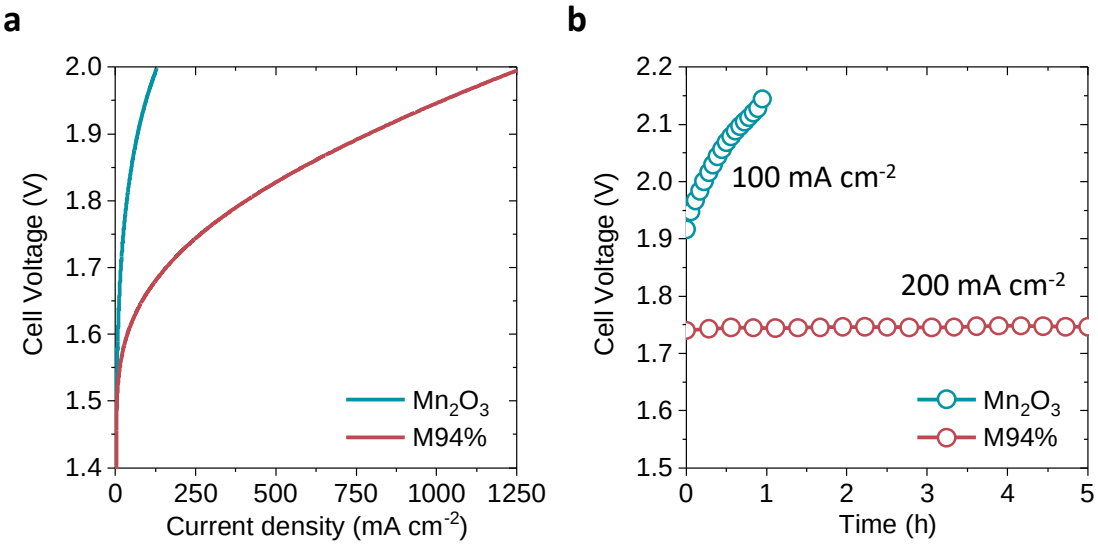

Supplementary Figure 16. Electrochemical performance of Mn_2O_3.
Polarization curves (**a**) and stability (**b**) of Mn_2O_3 evaluated in a PEM setup at 80 °C. The result of M94% is plotted together for comparison.

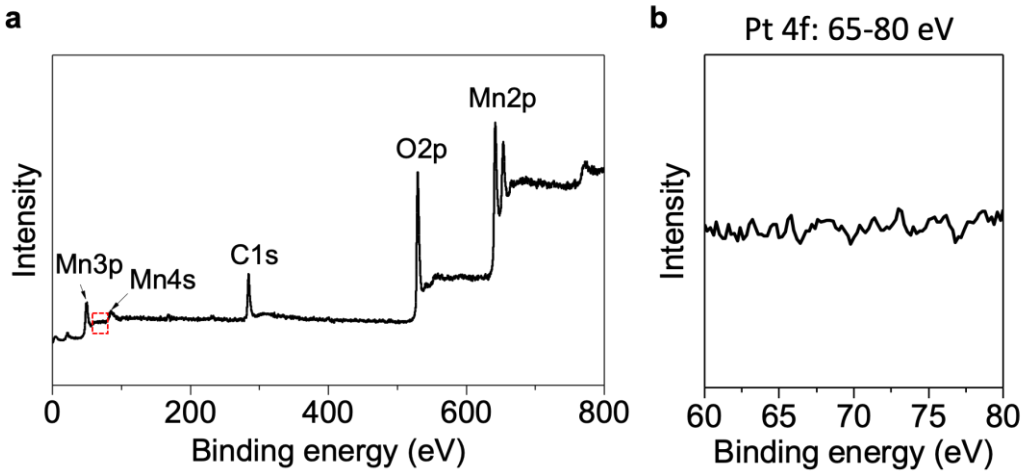

Supplementary Figure 17. XPS spectrum of γ-MnO_2 catalyst.
(**a**) XPS survey spectrum of the γ-MnO_2 catalyst. (**b**) The enlarged spectrum region (60 eV to 80 eV) of the red-marked rectangle in (**a**) shows Pt contamination on the surface of γ-MnO_2 was neglectable, which is under the detection limit of XPS.

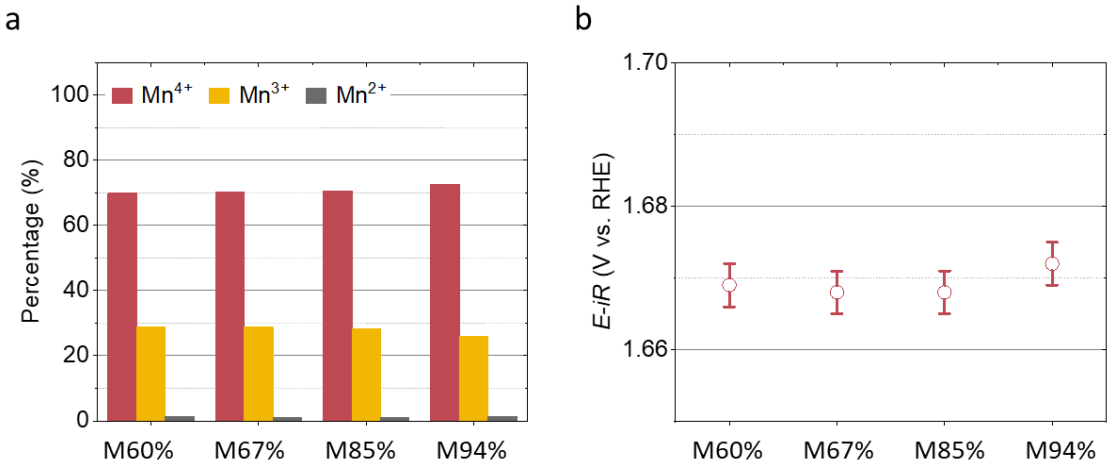

Supplementary Figure 18. The overpotentials of γ-MnO_2 catalysts at 10 mA cm^{-2}_{geo}. (**a**) Relative concentrations of the different oxidation states (Mn^{4+}, Mn^{3+}, Mn^{2+}) within the γ-MnO_2 catalysts obtained by fitting the $Mn2p_{3/2}$ XPS spectra. (**b**) The overpotentials of γ-MnO_2 catalysts at 10 mA cm^{-2}_{geo} in 1 M H_2SO_4 at 25 °C. Error bars show the standard deviation evaluated from at least three independent measurements.

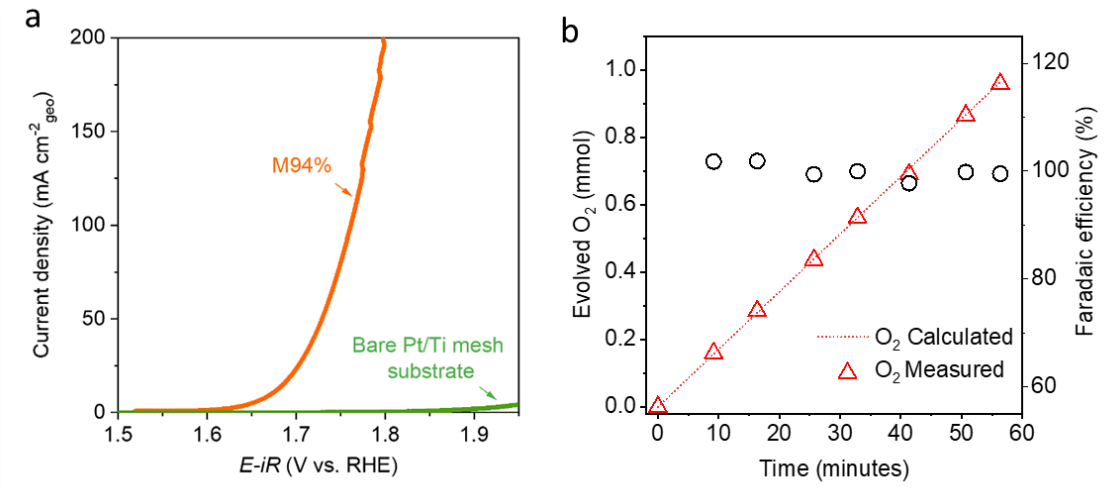

Supplementary Figure 19. Linear sweep voltammetry of Pt/Ti and Faradaic efficiency of γ-MnO_2.

(**a**) Linear sweep voltammetries of bare Pt/Ti mesh substrate and compared to that of M94% in 1 M H_2SO_4 as the electrolyte. The observed nearly zero OER activity of the bare substrate demonstrated that the current originated from the OER activity of the M94% catalyst. (**b**) Time course of the oxygen generated from water electrolysis at a constant current density of 200 mA cm^{-2}_{geo} in 1 M H_2SO_4 at 25 °C. The corresponding Faradaic efficiency is shown on a separate axis.

DFT studies on OER mechanism and active sites

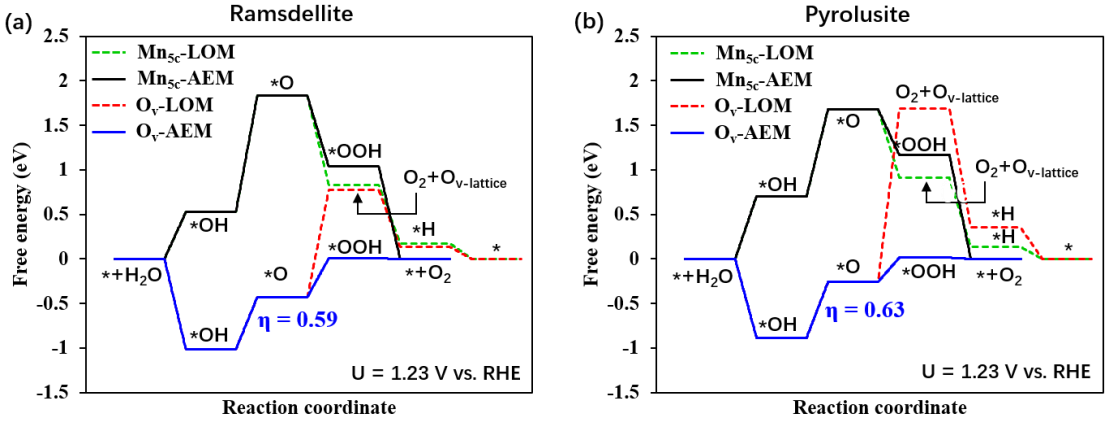

Supplementary Figure 20. Free energy diagrams of OER according to the AEM and LOM mechanisms.

DFT calculations were conducted to study the OER mechanisms on ramsdellite and pyrolusite structure units of γ-MnO_2 (M67%), respectively. For each of the units, two active sites were considered, namely the five-coordinate Mn (Mn_{5c}) and oxygen vacancy (O_v) site. For each of the active site, two reaction mechanisms, adsorbate evolution mechanism (AEM) and lattice oxygen mechanism (LOM), were considered (Supplementary Fig. 21 and 22 for the mechanism illustration). In the calculations of reaction free energies, the solvation energies of -0.11, -0.09, and -0.05 eV were adopted for species *OH, *O, and *OOH, respectively, which are obtained based on explicit and implicit water models (Supplementary Fig. 23 and Supplementary Table 8). The above figures show the free energy diagram of OER with AEM and LOM mechanisms on Mn_{5c} and O_v side of ramsdellite (**a**) and pyrolusite (**b**) phases at 1.23 V vs. RHE. Three main conclusions can be drawn from this figure: (1) The O_v sites on ramsdellite and pyrolusite phases are the active sites of γ-MnO_2 for OER. (2) On O_v sites of ramsdellite and pyrolusite units, the AEM mechanism is more favorable than LOM. (3) The OER activity of ramsdellite and pyrolusite phase is nearly the same because their overpotentials (η) are very close (0.59 and 0.63 V, respectively), which can support the experimental results that the activity of γ-MnO_2 didn't change with the O_{pla} concentration.

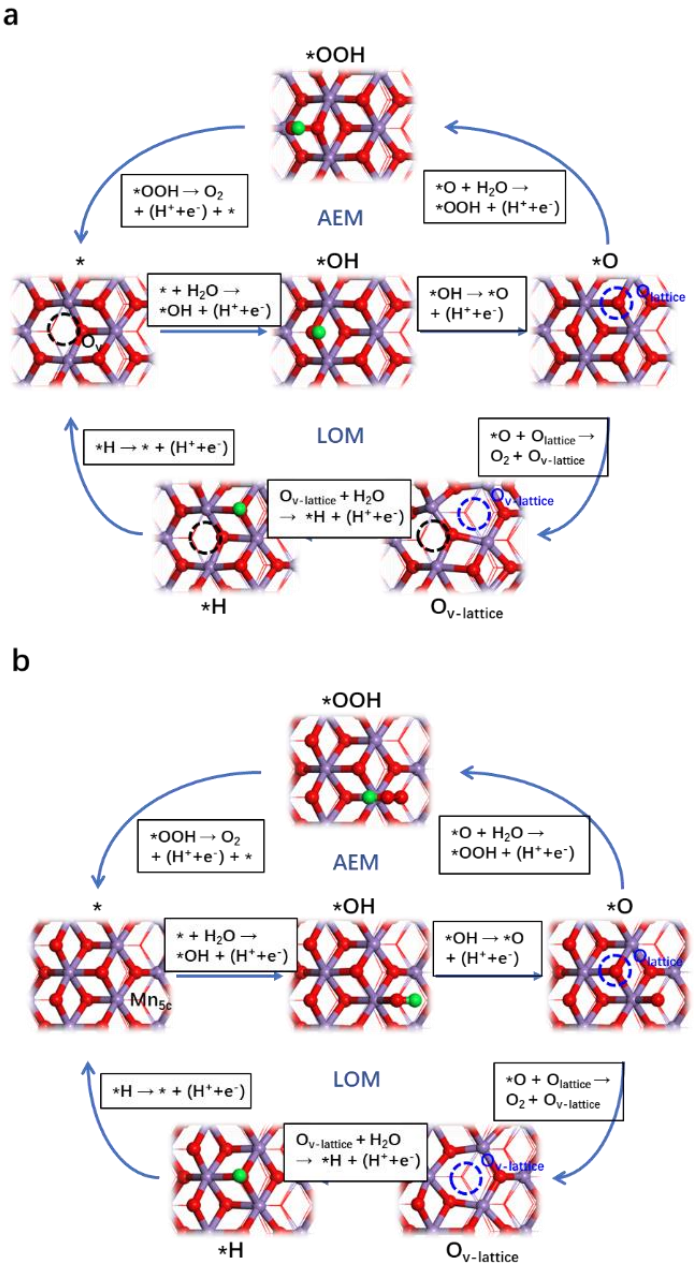

Supplementary Figure 21. AEM and LOM mechanism illustration on ramsdellite structure unit.

Mechanistic illustration and optimized structures of intermediates in the adsorbate evolution mechanism (AEM) and lattice oxygen mediated mechanism (LOM) on ramsdellite (**a**) O_v site and (**b**) Mn_{5c} site.

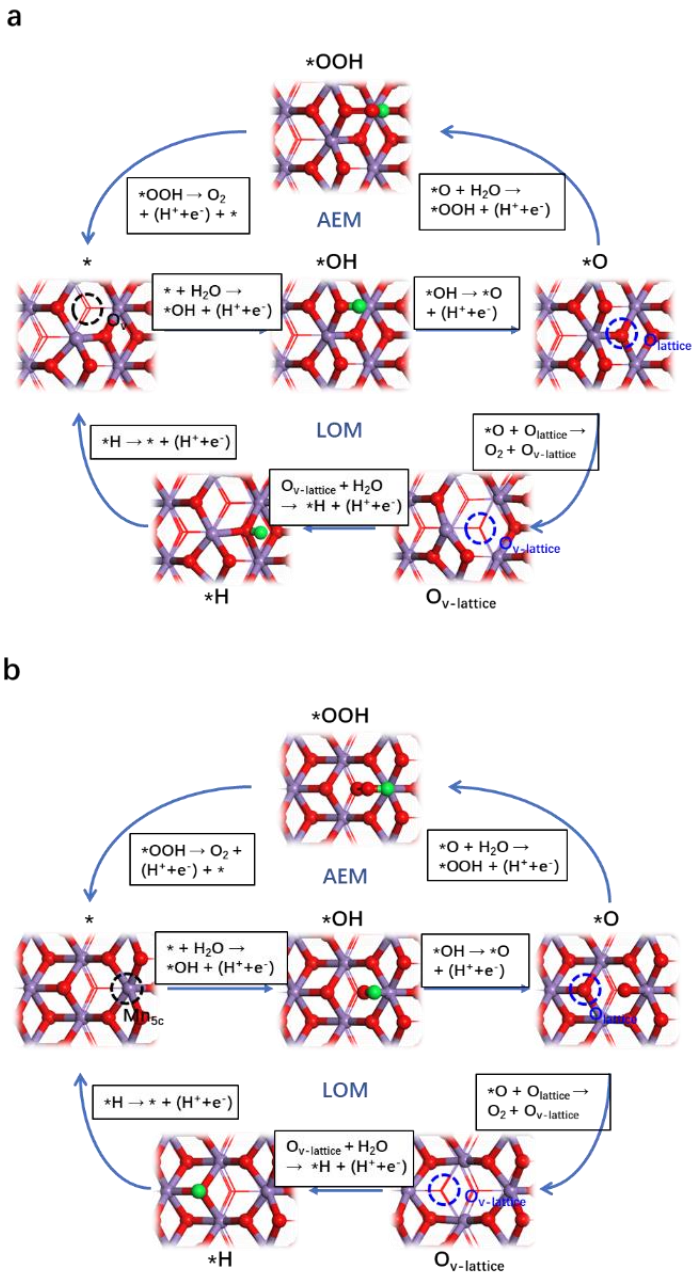

Supplementary Figure 22. AEM and LOM mechanism illustration on pyrolusite structure unit.

Mechanistic illustration and optimized structures of intermediates in the adsorbate evolution mechanism (AEM) and lattice oxygen mediated mechanism (LOM) on pyrolusite (**a**) O_v site and (**b**) Mn_{5c} site.

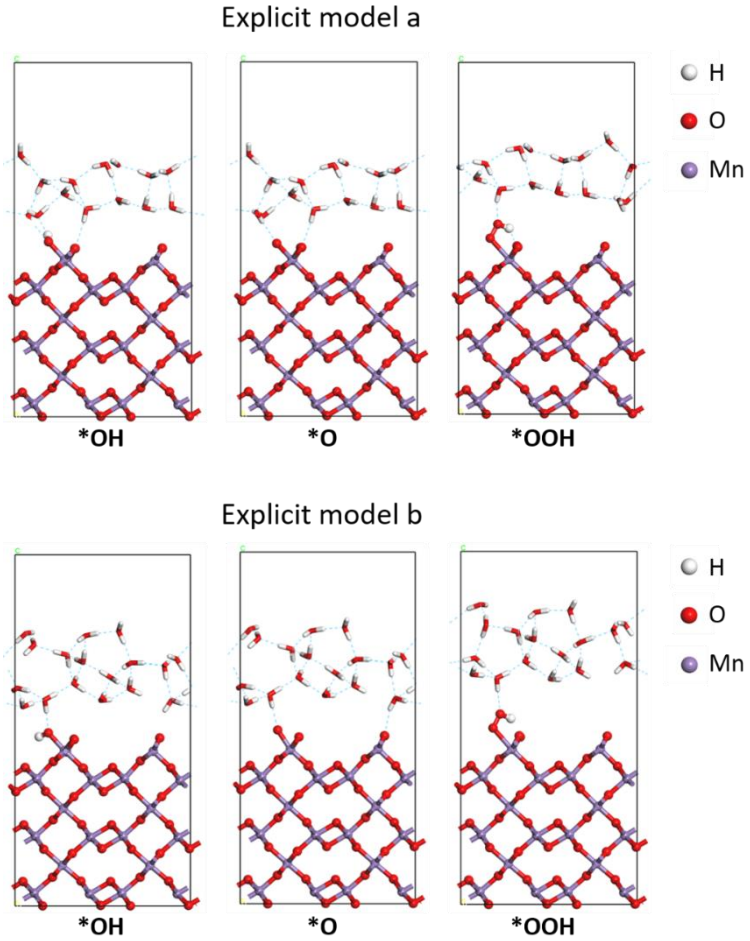

Supplementary Figure 23. Structures of explicit water model for the calculations of solvation energies.

Two different explicit water models (a and b) were applied on γ-MnO_2 (M67%) surface to estimate the solvation energies. We first calculated the adsorption of intermediates in the presence of water layer, then the intermediates were removed and the γ-MnO_2 slab with water were optimized. Thus, the adsorption energies under explicit solvent can be calculated. Considering the uncertainty of explicit water layer structure, the solvation energies were also examined based on the implicit method (VASPsol)[11]. Supplementary Table 8 lists the solvation energies calculated with explicit model a, b, and implicit model. All three models yield similar results within an error margin of less than 0.1 eV. Despite using values from different models or averaged values, our conclusion remains unchanged: the dissolution from an O_{pla} site is unfavorable than from an O_{pyr} site. In the revised manuscript, we have adopted the averaged values of solvation energies to account for variations in the water layer structure: *OH (-0.11 eV), *O (-0.09 eV), and *OOH (-0.05 eV).

Electrochemical Performance

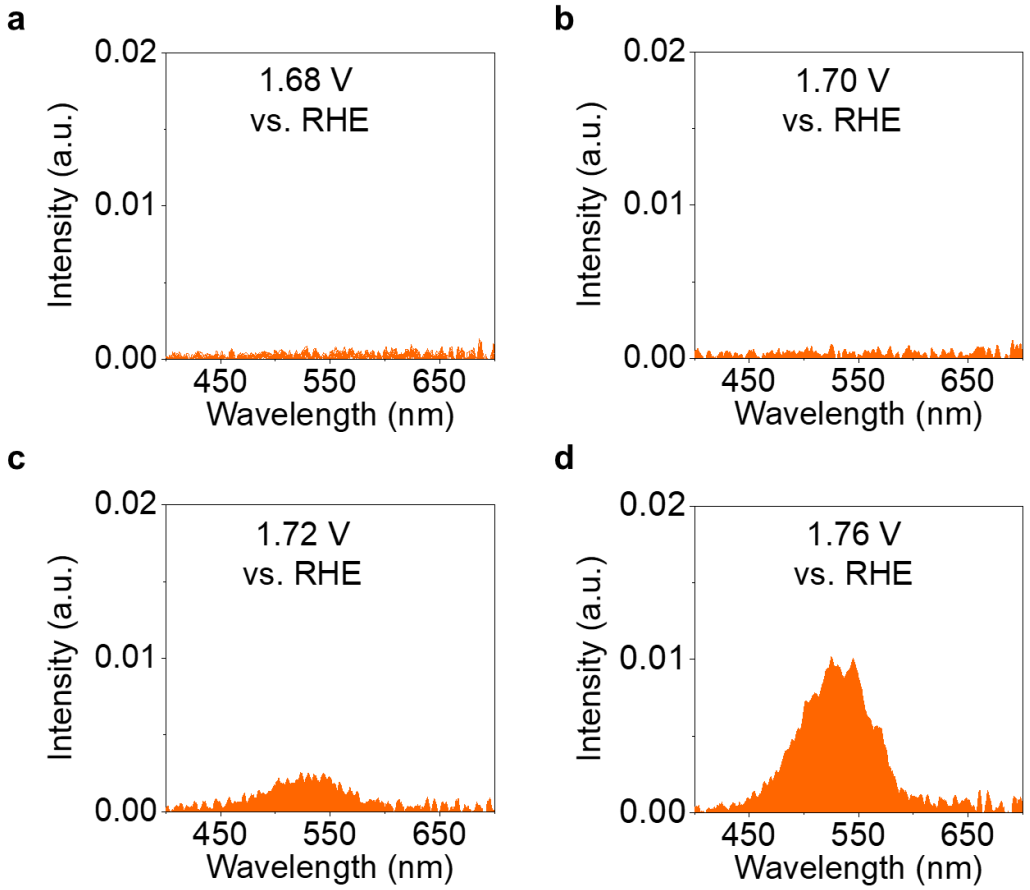

Supplementary Figure 24. UV-Vis measurement of MnO_4^- formation from M60%. UV-Vis absorption spectra of the electrolyte (1 M H_2SO_4) after 30 min of electrolysis at (**a**) 1.68, (**b**) 1.70, (**c**) 1.72, and (**d**) 1.76 V vs. RHE for the M60% sample. Only when the potential was increased to approximately 1.72 V vs. RHE were new absorption peaks observed at 525 and 545 nm. These absorption peaks are the absorption features of $Mn^{VII}O_4^-$, indicating the dissolution of the M60% electrode initiated at potentials around 1.72 V vs. RHE.

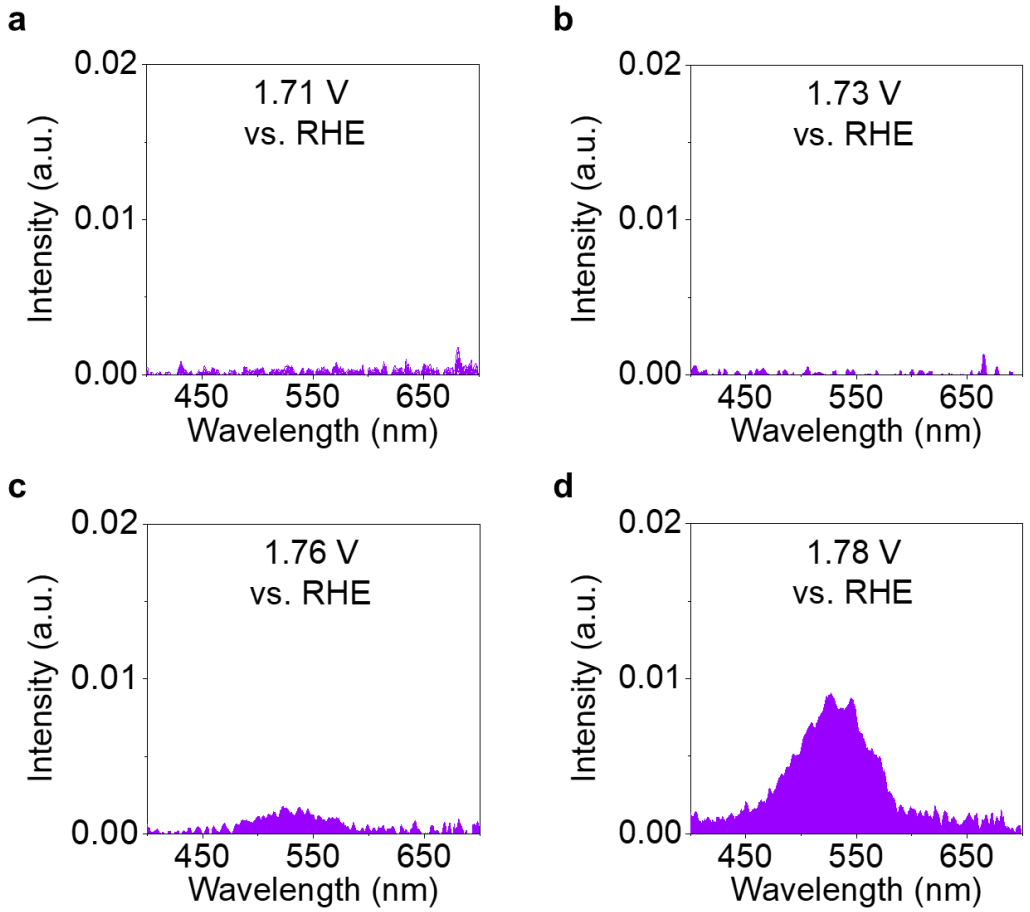

Supplementary Figure 25. UV-Vis measurement of MnO_4^- formation from M67%. UV-Vis absorption spectra of the electrolyte (1 M H_2SO_4) after 30 min of electrolysis at (**a**) 1.71, (**b**) 1.73, (**c**) 1.76, and (**d**) 1.78 V vs. RHE for the M67% sample. Only when the potential was increased to approximately 1.76 V vs. RHE were new absorption peaks observed at 525 and 545 nm. These absorption peaks are the absorption features of $Mn^{VII}O_4^-$, indicating the dissolution of the M67% electrode initiated at potentials around 1.76 V vs. RHE.

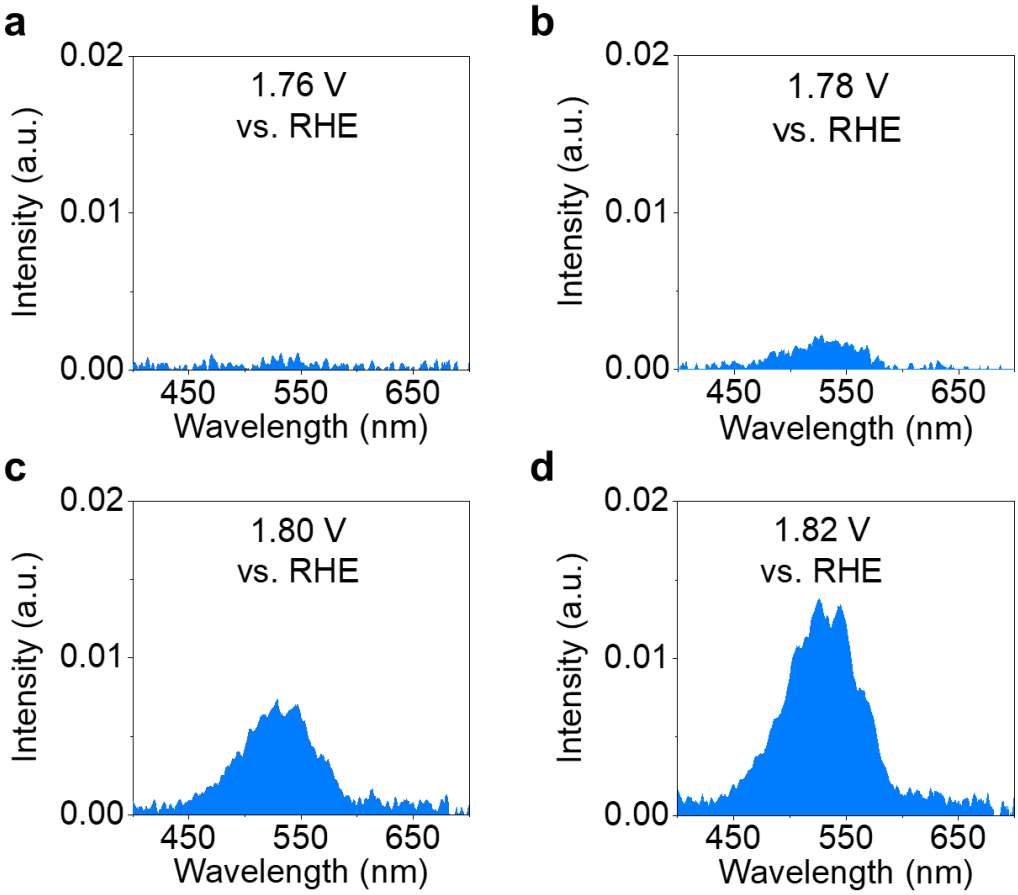

Supplementary Figure 26. UV-Vis measurement of MnO_4^- formation from M85%. UV-Vis absorption spectra of the electrolyte (1 M H_2SO_4) after 30 min of electrolysis at (**a**) 1.76, (**b**) 1.78, (**c**) 1.80, and (**d**) 1.82 V vs. RHE for the M85% sample. Only when the potential was increased to approximately 1.78 V vs. RHE were new absorption peaks observed at 525 and 545 nm. These absorption peaks are the absorption features of $Mn^{VII}O_4^-$, indicating the dissolution of the M85% electrode initiated at potentials around 1.78 V vs. RHE.

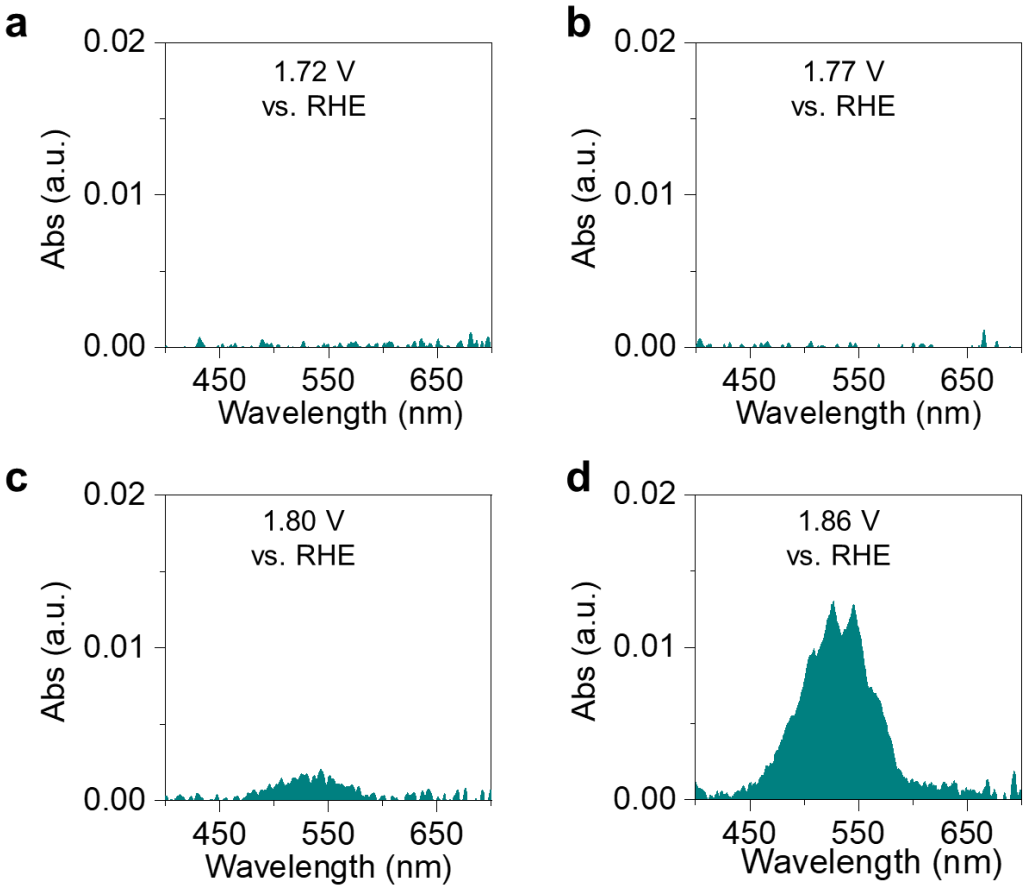

Supplementary Figure 27. UV-Vis measurement of MnO_4^- formation from M94%. UV-Vis absorption spectra of the electrolyte (1 M H_2SO_4) after 30 min of electrolysis at (**a**) 1.72, (**b**) 1.77, (**c**) 1.80, and (**d**) 1.86 V vs. RHE for the M94% sample. Only when the potential was increased to approximately 1.80 V vs. RHE were new absorption peaks observed at 525 and 545 nm. These absorption peaks are the absorption features of $Mn^{VII}O_4^-$, indicating the dissolution of the M94% electrode initiated at potentials around 1.80 V vs. RHE.

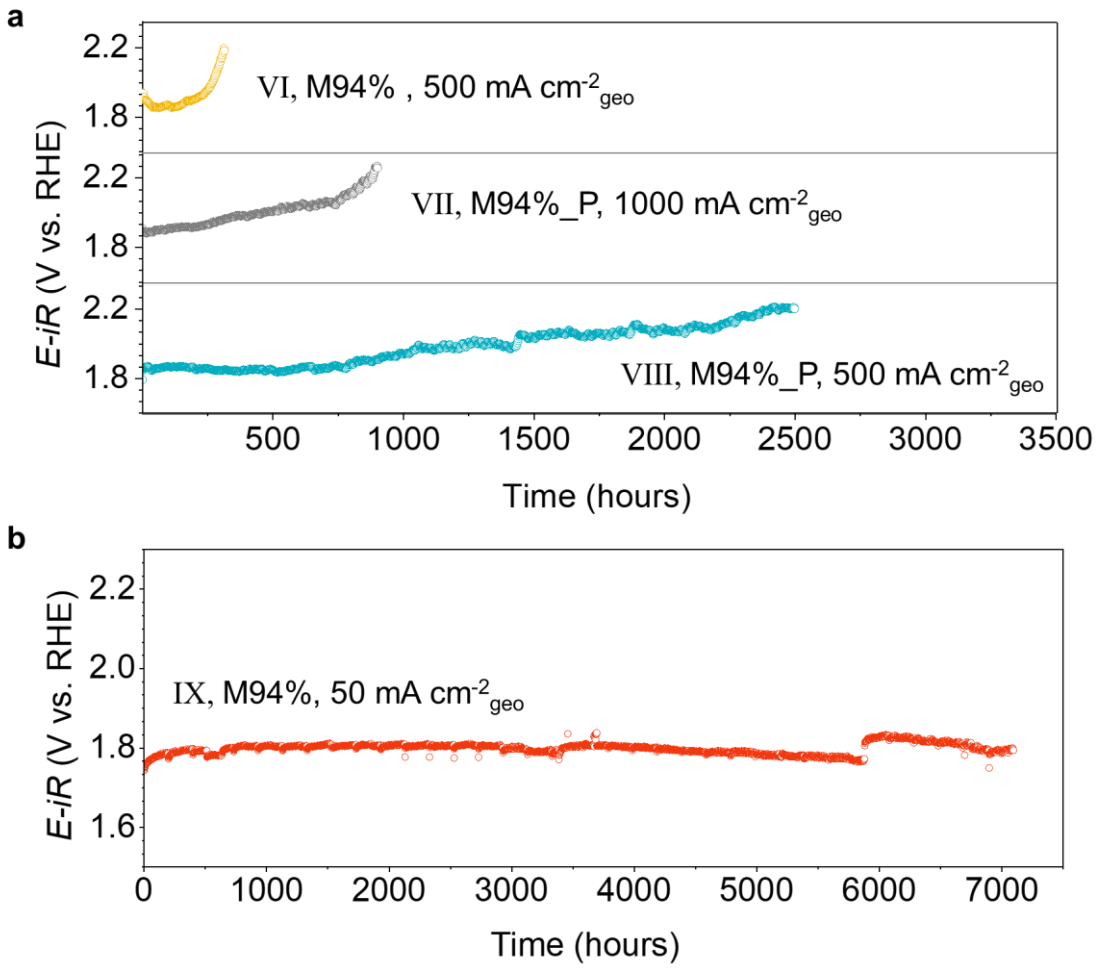

Supplementary Figure 28. Chronopotentiometry of M94% and M94%_P.
(**a**) Chronopotentiometry of M94% at 500 mA cm^{-2}_{geo} and M94%_P at 1000 and 500 mA cm^{-2}_{geo}. (**b**) Chronopotentiometry of M94% at 50 mA cm^{-2}_{geo}. The roman numerals VI, VII, VIII, and IX here are to show that the curve is corresponded to the data point in Fig. 3b labeled with same roman numeral.

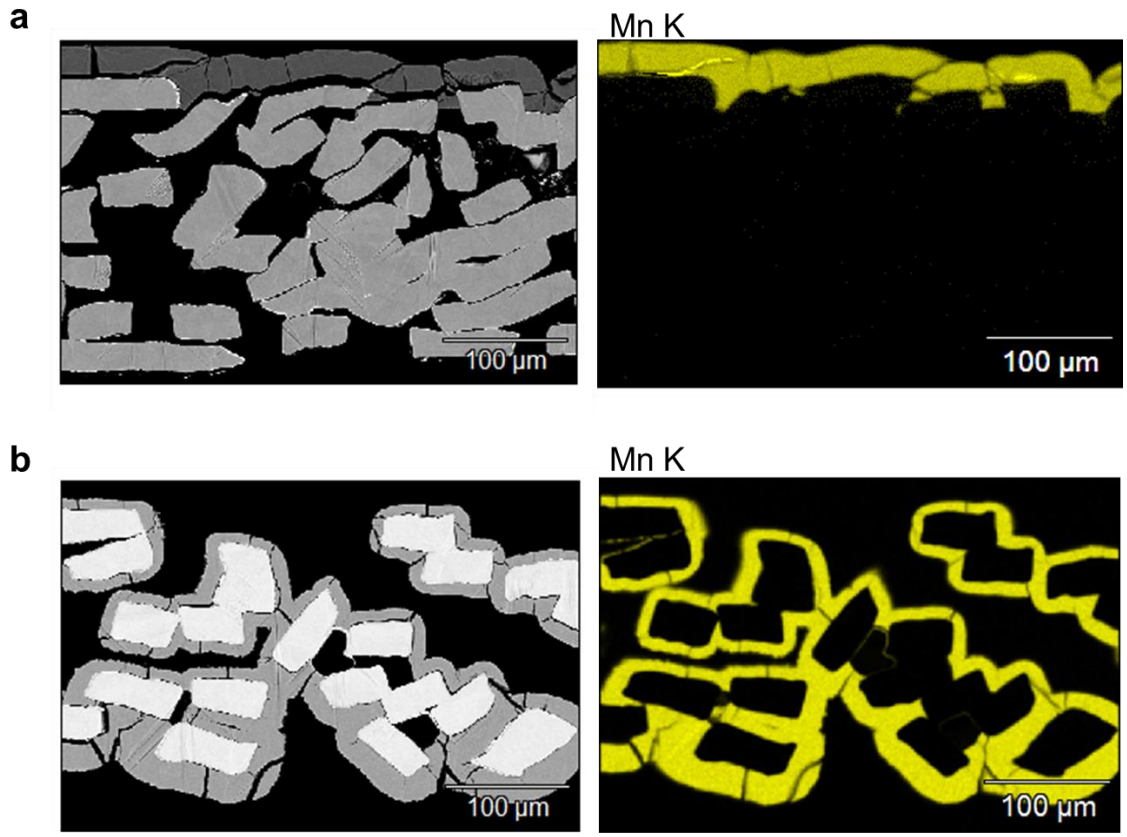

Supplementary Figure 29. Cross-sectional images of the γ-MnO_2 electrode.
Cross-sectional scanning electron microscopy images of the electrode with γ-MnO_2 catalyst deposited on Pt/Ti mesh prepared by an electrodeposition method. (**a**) Electrodeposition with stationary electrolyte. γ-MnO_2 catalyst was deposited on the top surface of Pt/Ti mesh. (**b**) Electrodeposition with electrolyte pumping into the Pt/Ti mesh. The γ-MnO_2 catalyst was deposited uniformly, wrapping almost all the Pt/Ti fibers. Scale bar, 100 μm.

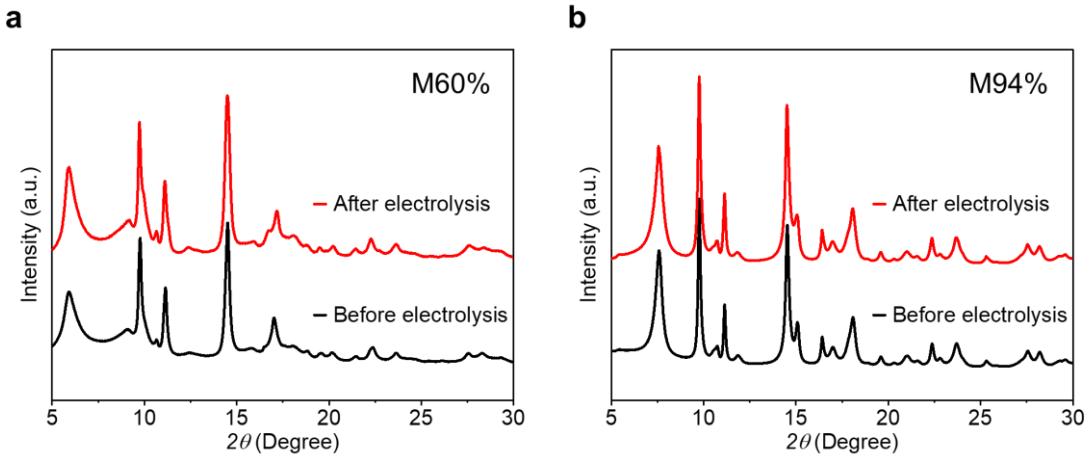

Supplementary Figure 30. SR-PXRD patterns of M60% and M94% after electrolysis.
SR-PXRD patterns of M60% (**a**) and M94% (**b**) before and after electrolysis at 200 mA cm^{-2}_{geo} for 40 hours in pH 1 H_2SO_4 at 25 °C.

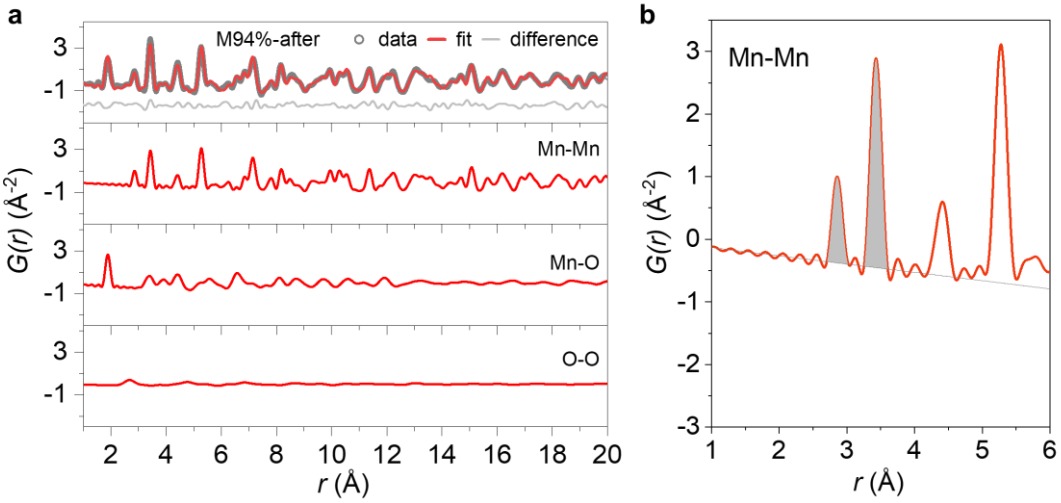

c

A1	r1	A2	r2	Mn-Mn$_{corner}$ ratio	O$_{pla}$ Concentration
0.627	3.430	0.234	2.858	76.32%	93.87%

Supplementary Figure 31. Pair distribution function of M94% after electrolysis. (**a**) Refinement of the pair distribution function (PDF) of M94% after electrolysis for 40 h at 200 mA cm^{-2}_{geo} (M94%-after), as well as the decomposition of the fitted PDF into contributions from the Mn-Mn (Mn-Mn partial PDF), Mn-O (Mn-O partial PDF), and O-O (O-O partial PDF) atom pairs. (**b**) Integration of the Mn-Mn$_{edge}$ and Mn-Mn$_{corner}$ peaks in Mn-Mn partial PDF (shaded area). The grey lines indicate baselines that are based on the definition of $G(r)$, $G(r) = 4\pi\rho_0 r(g(r)-1)$. As $r \rightarrow +0$, this function behaves like $-4\pi\rho_0 r$ and passes through zero with a slope that is proportional to the average number density (ρ_0) of the material. The percentage of Mn-Mn$_{corner}$ was calculated as $A_1 \times r_1/(A_1 \times r_1 + A_2 \times r_2)$, where A_1 and A_2 are the integrated peak area of Mn-Mn$_{corner}$ and Mn-Mn$_{edge}$, and r_1 and r_2 are the corresponding peak positions. (**c**) Parameters for peak integration.

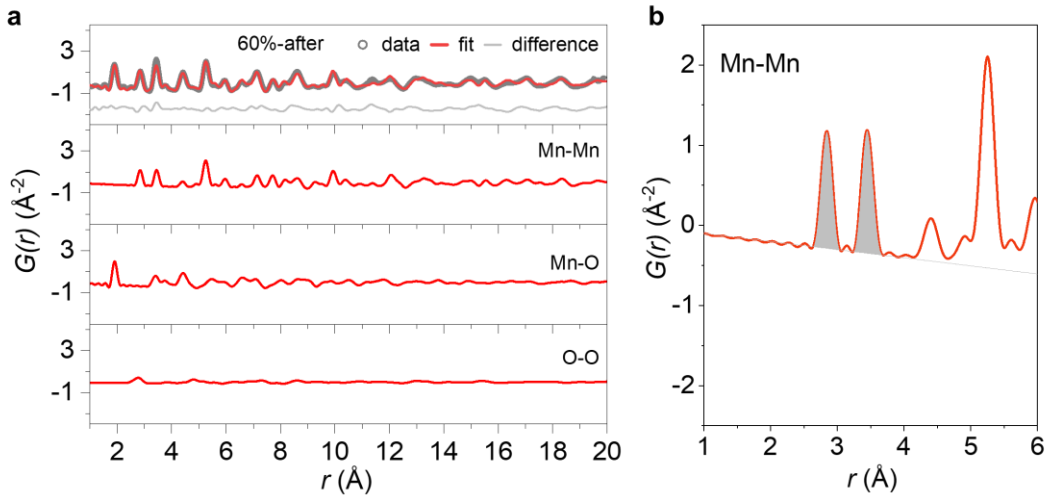

c

A1	r1	A2	r2	Mn-Mn$_{corner}$ ratio	O$_{pla}$ concentration
0.320	3.447	0.295	2.842	56.83%	61.38%

Supplementary Figure 32. Pair distribution function of M60% after electrolysis. (**a**) Refinement of the pair distribution function (PDF) of M60% after electrolysis for 40 h at 200 mA cm$^{-2}_{geo}$ (M60%-after), as well as the decomposition of the fitted PDF into contributions from the Mn-Mn (Mn-Mn partial PDF), Mn-O (Mn-O partial PDF), and O-O (O-O partial PDF) atom pairs. (**b**) Integration of the Mn-Mn$_{edge}$ and Mn-Mn$_{corner}$ peaks in Mn-Mn partial PDF (shaded area). The grey lines indicate baselines that are based on the definition of $G(r)$, $G(r) = 4\pi\rho_0 r(g(r)-1)$. As $r \rightarrow +0$, this function behaves like $-4\pi\rho_0 r$ and passes through zero with a slope that is proportional to the average number density (ρ_0) of the material. The percentage of Mn-Mn$_{corner}$ was calculated as $A_1 \times r_1/(A_1 \times r_1 + A_2 \times r_2)$, where A_1 and A_2 are the integrated peak area of Mn-Mn$_{corner}$ and Mn-Mn$_{edge}$, and r_1 and r_2 are the corresponding peak positions. (**c**) Parameters for peak integration.

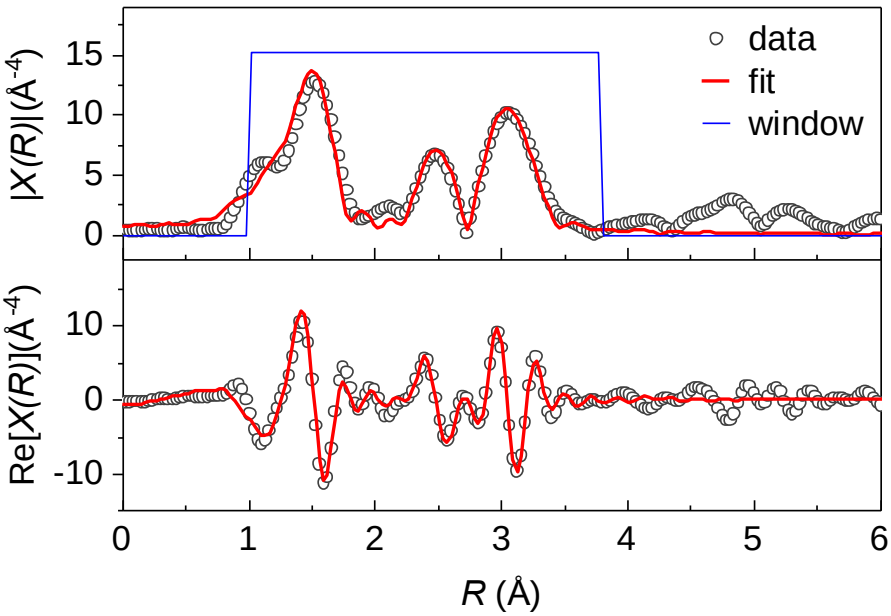

Supplementary Figure 33. Mn K-edge EXAFS measurement of M94% after electrolysis.
Fitting analysis of Fourier-transformed k^3-weighted Mn K-edge EXAFS measurement of M94% after electrolysis at 200 mA cm^{-2}_{geo} in 1 M H_2SO_4. The fitting was conducted within the *R* range of 1-3.8 Å, and optimized parameters can be found in Supplementary Table 10. The upper panel shows the magnitude of FT-EXAFS, and the lower panel shows its real part. Detailed procedures for fitting are provided in **Methods**.

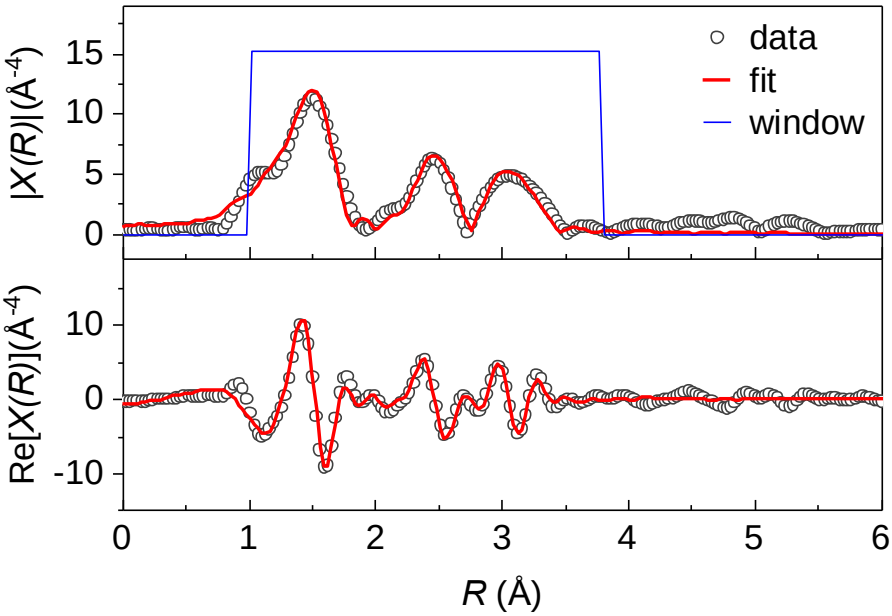

Supplementary Figure 34. Mn K-edge EXAFS measurement of M60% after electrolysis.
Fitting analysis of Fourier-transformed k^3-weighted Mn K-edge EXAFS measurement of M60% after electrolysis at 200 mA cm^{-2}_{geo} in 1 M H_2SO_4. The fitting was conducted within the *R* range of 1-3.8 Å, and optimized parameters can be found in Supplementary Table 11. The upper panel shows the magnitude of FT-EXAFS, and the lower panel shows its real part. Detailed procedures for fitting are provided in **Methods**.

DFT Studies on γ-MnO_2 Stability

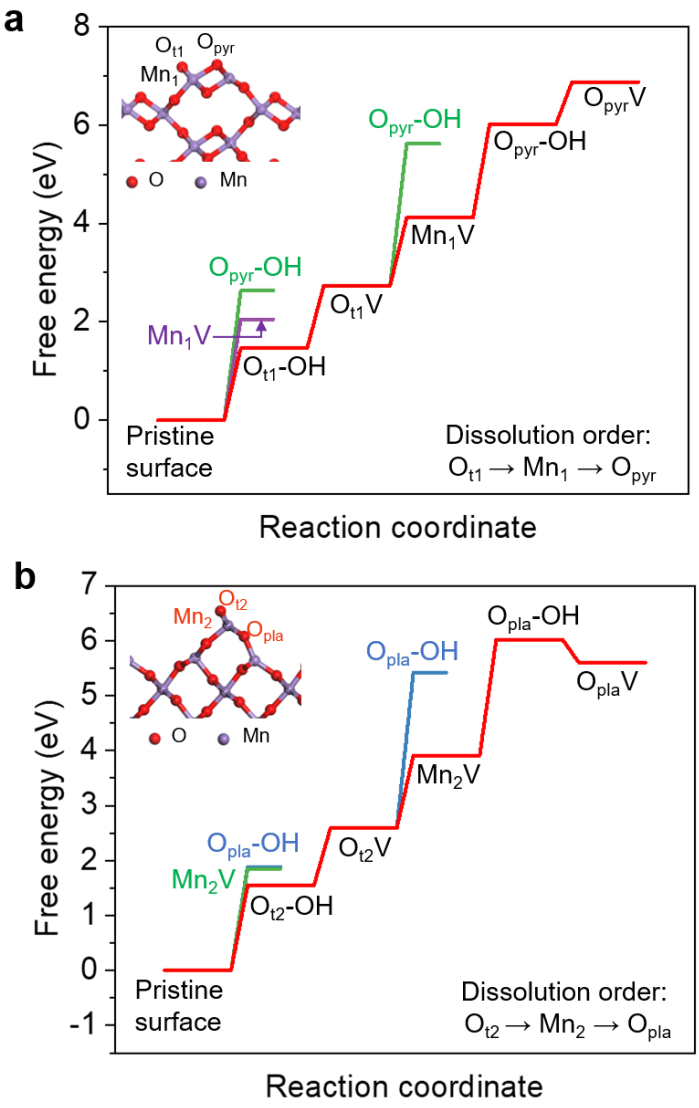

Supplementary Figure 35. Free energy diagram of γ-MnO_2 dissolution.
Free energy diagram of catalyst dissolution through (**a**) O_{pyr} mechanism at M50% (001) surface and (**b**) O_{pla} mechanism at M100% (100) surface. The red line represents the optimal dissolution pathway. The inserts in **a** and **b** show the pristine surface structures of each model and atoms involved in the elementary steps were indicated.

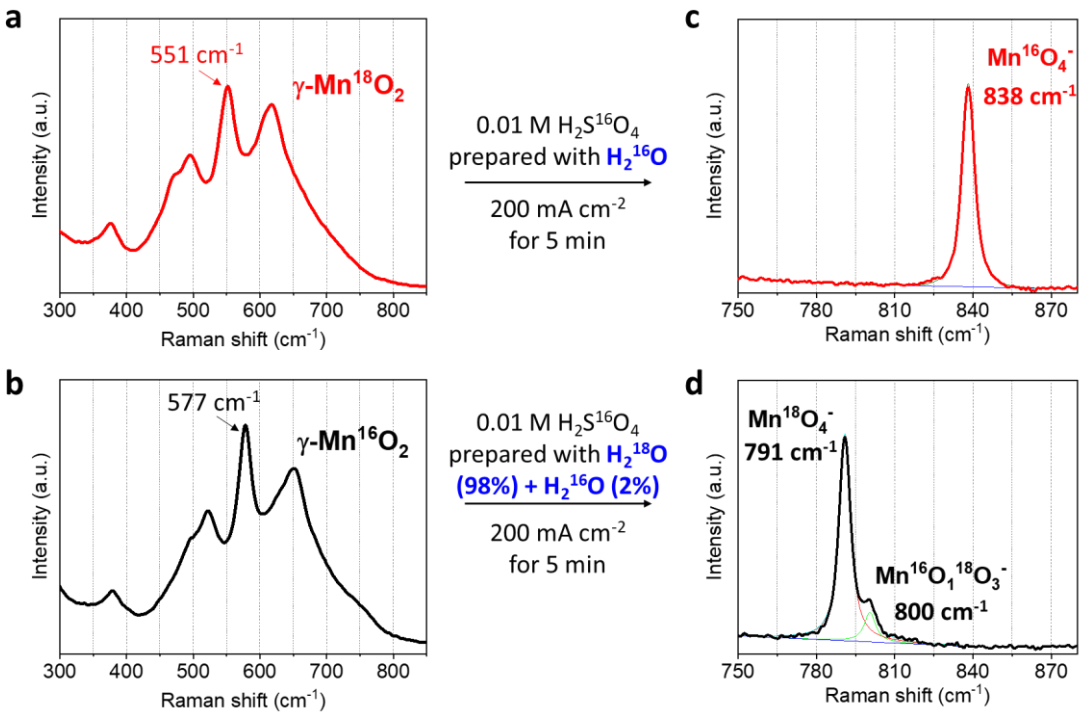

Supplementary Figure 36. ^{18}O isotopic labeling of γ-MnO_2 dissolution measured with Raman.
Raman spectra of γ-$Mn^{18}O_2$ (**a**) and γ-$Mn^{16}O_2$ (**b**): Three peaks characteristic to γ-$Mn^{16}O_2$ shifted to a higher wavenumber by approximately 26 cm^{-1} by substituting lattice oxygen from ^{16}O to ^{18}O (Refs[12,13]). Raman spectra of permanganate ($Mn^{VII}O_4^-$) generated as a dissolution product after 5 min of electrolysis at 200 mA cm^{-2} in 0.01 M H_2SO_4 (**c** and **d**): When the electrolysis was conducted using γ-$Mn^{18}O_2$ in 0.01 M $H_2S^{16}O_4$ electrolyte, only ^{16}O-permanganate was formed (**c**). No formation of ^{18}O-contaning permanganate suggests that lattice oxygen of γ-$Mn^{18}O_2$ is not involved in the metal dissolution pathway. When the electrolysis was conducted using γ-$Mn^{16}O_2$ in 0.01 M $H_2S^{18}O_4$ prepared with $H_2{}^{18}O$ (98%) + $H_2{}^{16}O$ (2%), ^{18}O-contaning permanganate was generated as a main product (**d**). The product ratio of $Mn^{16}O_1{}^{18}O_3^-$ (8.5% ± 1.6%) and $Mn^{18}O_4^-$ (91.5% ± 1.6%) corresponds to a total amount of 2.1% ± 0.4% ^{16}O in dissolved permanganate, which is consistent with the original concentration of $H_2{}^{16}O$ (2%) in the electrolyte. Consistency of the $^{16}O/^{18}O$ isotope ratio of permanganate and electrolyte solutions further supports that the metal dissolution proceeds primarily without the involvement of lattice oxygen. Therefore, the leaching of metal and oxygen was considered separately in DFT calculations (Supplementary Table 12).

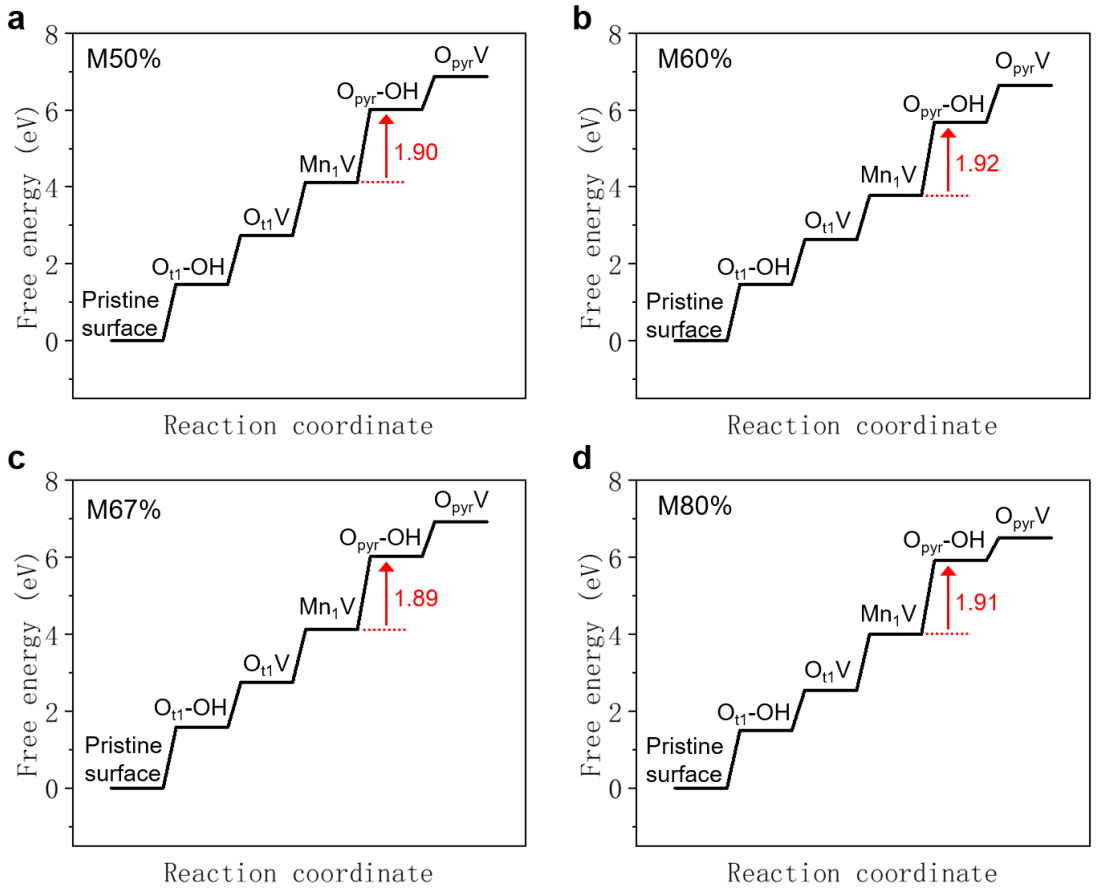

Supplementary Figure 37. Dissolution through O_{pyr} mechanism with different O_{pla} concentrations.
Free energy diagrams for dissolution through O_{pyr} mechanism in MnO_2 with O_{pla} concentrations of (**a**) 50%, (**b**) 60%, (**c**) 67%, and (**d**) 80%. The potential-determining steps (PDS) are marked by red arrows. The reaction free energy of each elementary step is listed in Supplementary Table 12.

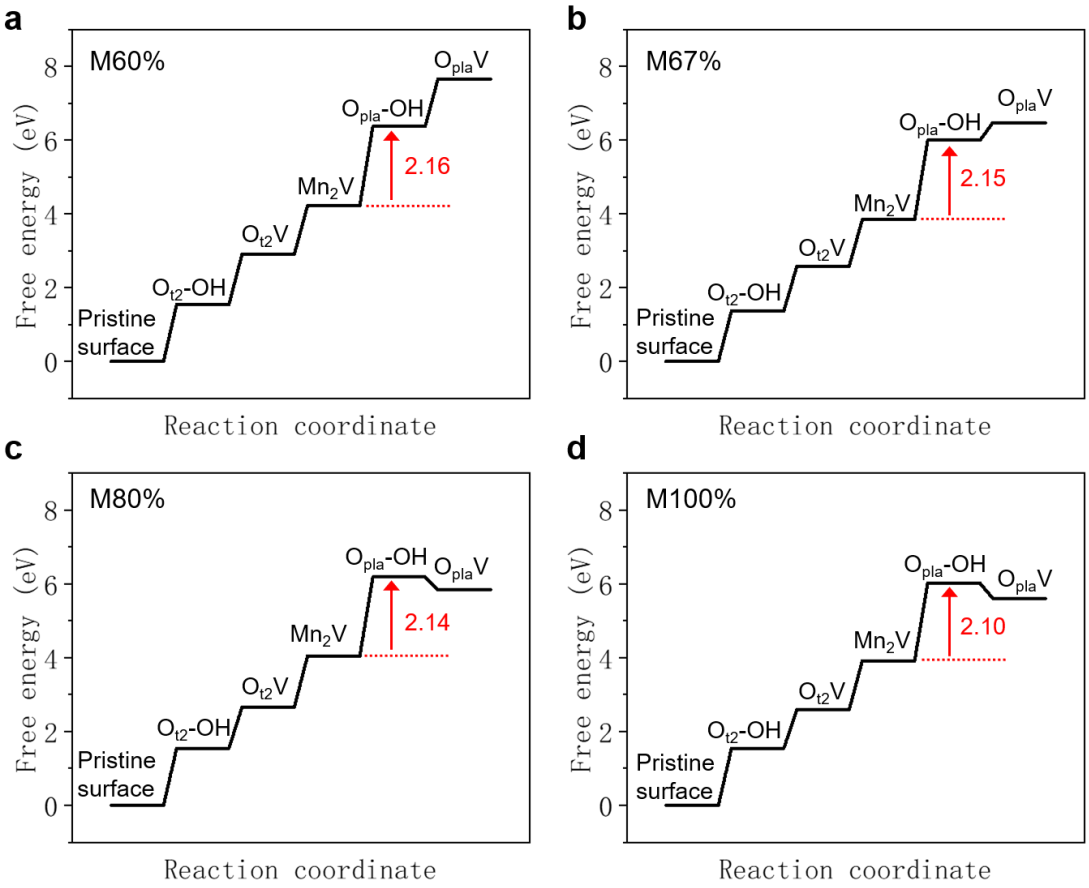

Supplementary Figure 38. Dissolution through O_{pla} mechanism with different O_{pla} concentrations.
Free energy diagrams for dissolution through O_{pla} mechanism in MnO_2 with O_{pla} concentrations of (**a**) 60%, (**b**) 67%, (**c**) 80%, and (**d**) 100%. The potential-determining steps (PDS) are marked by red arrows. The reaction free energy of each elementary step is listed in Supplementary Table 12.

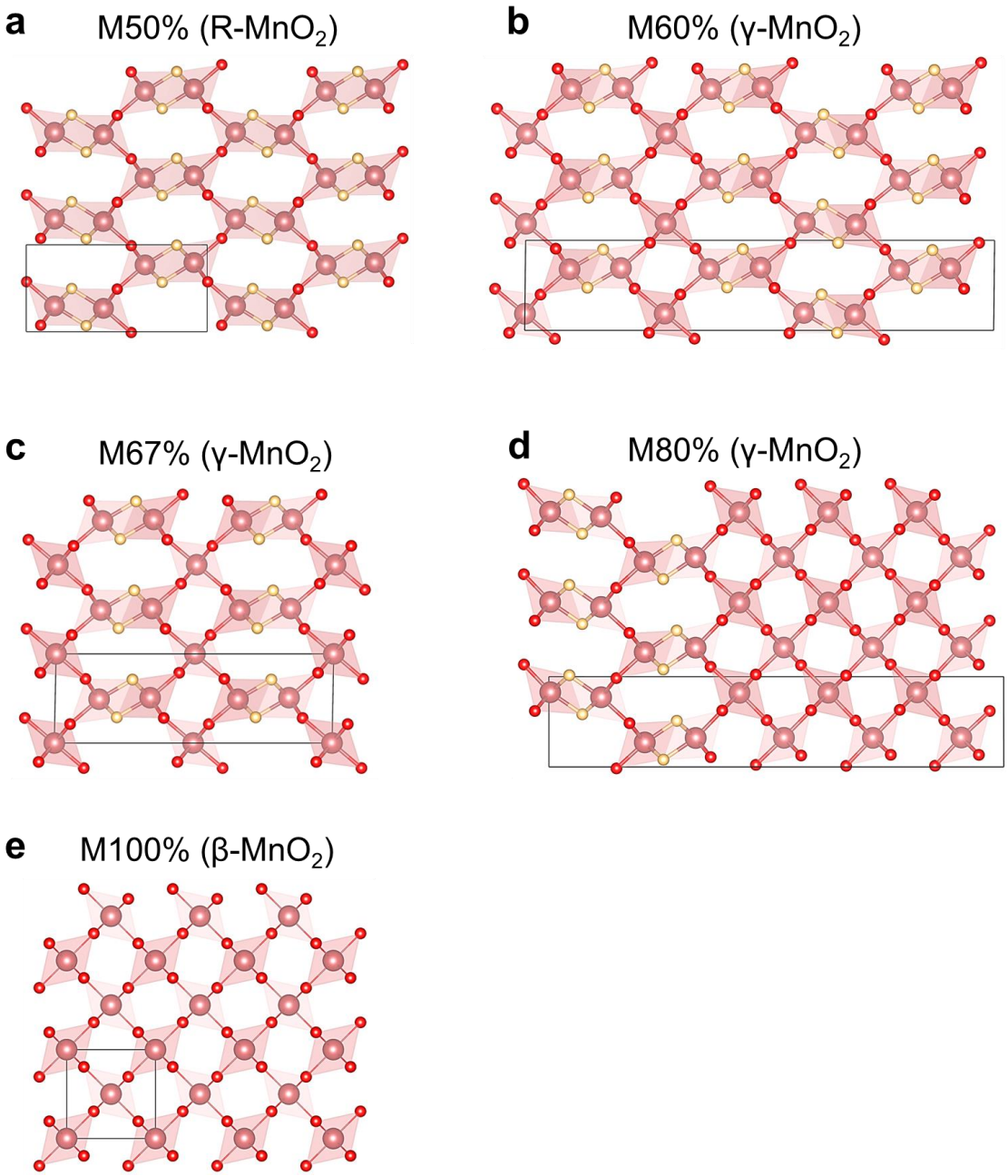

Supplementary Figure 39. Bulk structures of MnO_2 with different O_{pla} concentrations.
Atomic models of MnO_2 bulk with O_{pla} concentrations of (**a**) 50%, (**b**) 60%, (**c**) 67%, (**d**) 80%, and (**e**)100%. The red and yellow small balls represent O_{pla} and O_{pyr}, respectively. The big balls represent Mn atoms. The black lines represent lattice.

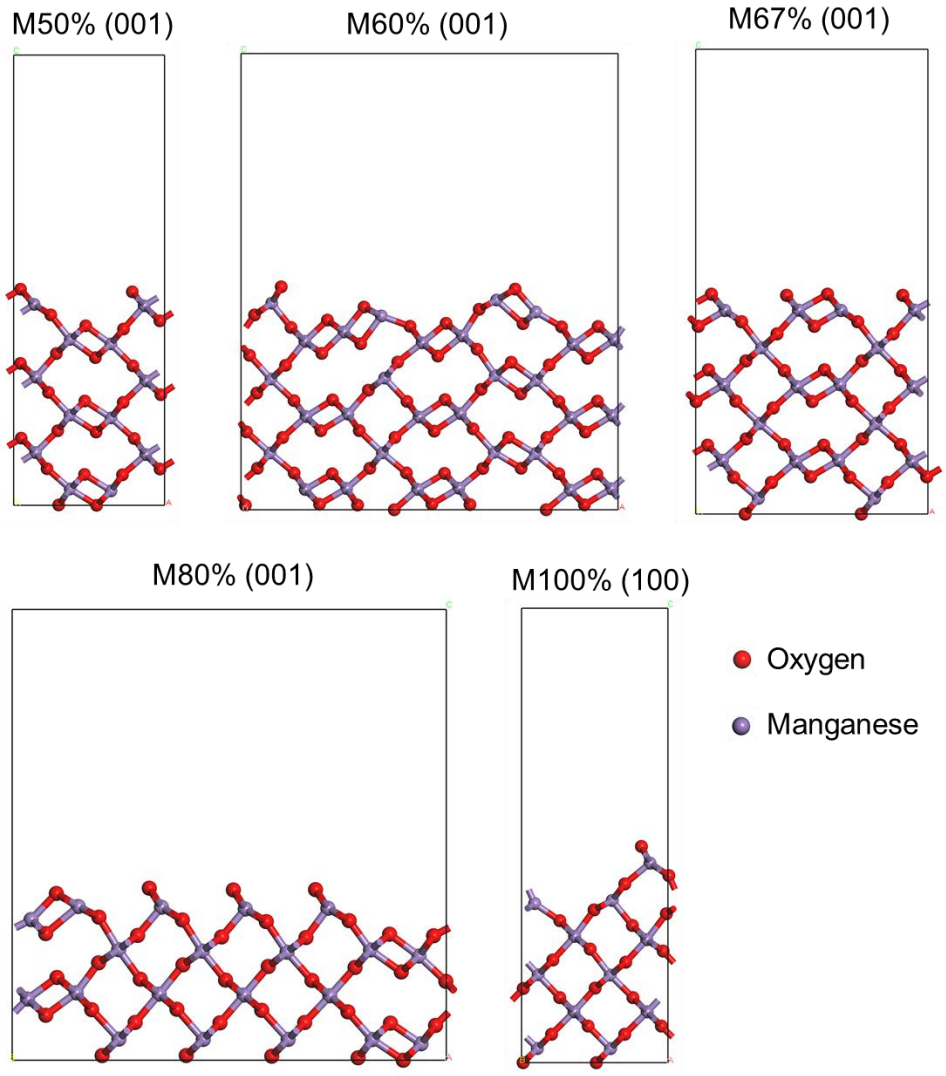

Supplementary Figure 40. Atomic structures of cleaved surfaces for different MnO_2. Atomic structures of cleaved surfaces for different MnO_2. A vacuum of ~15 Å was added to the surfaces to avoid the interaction between adjacent slabs.

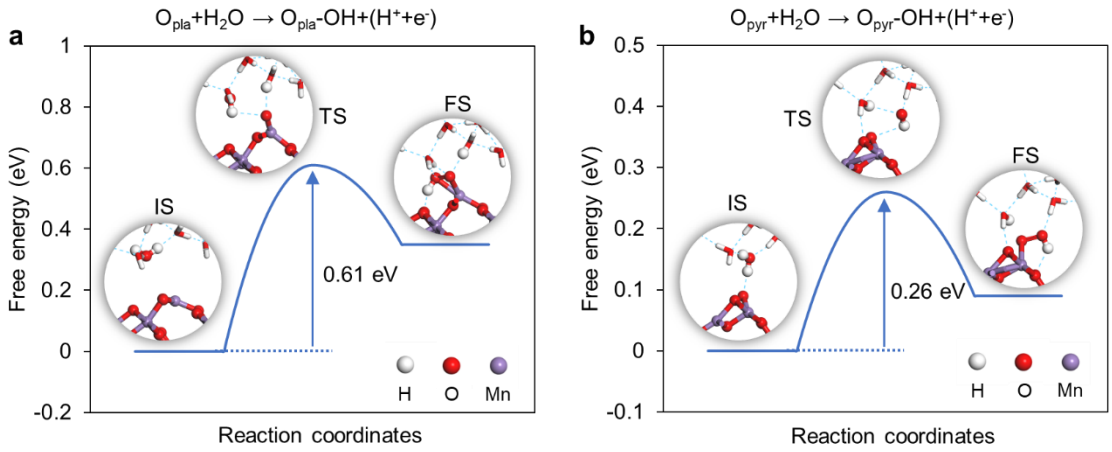

Supplementary Figure 41. Free energy diagram and local structures of initial (IS), transition (TS), and final state (FS) for hydroxylation of (a) O_{pla} and (b) O_{pyr}.

The climbing-image nudged elastic band (CI-NEB) method was adopted to search the transition states for O_{pla} and O_{pyr} hydroxylation. A charge extrapolation scheme was used to estimate the corresponding electrochemical barriers at constant potential, which are 0.61 and 0.26 eV at 1.8 V vs. RHE for (**a**) O_{pla} and (**b**) O_{pyr} hydroxylation, respectively. The details of the charge extrapolation method can be found in previous literatures[14,15].

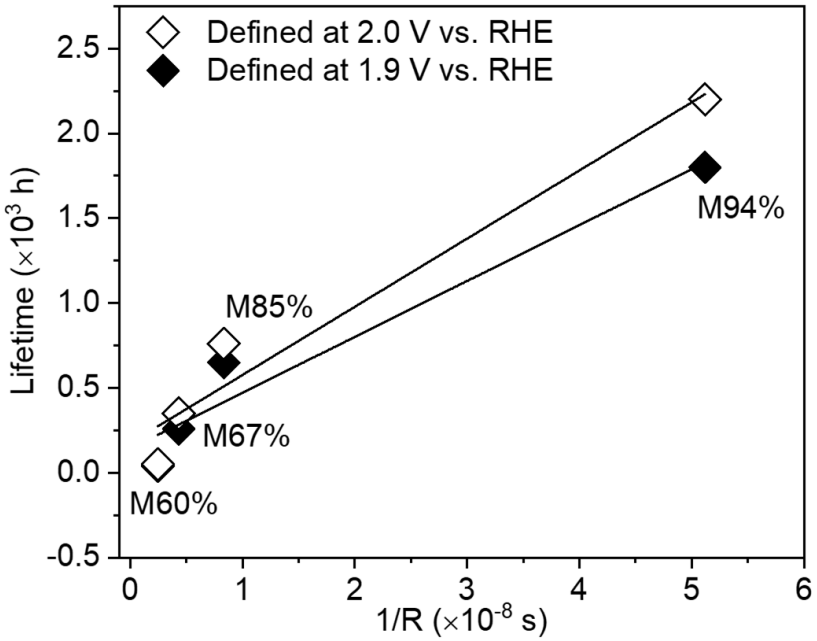

Supplementary Figure 42. Theoretical dissolution rate of γ-MnO_2 versus experimental lifetime.
The reciprocal of theoretical dissolution rate (R) of γ-MnO_2 versus experimental lifetime in the three-electrode system. The solid and void diamond represent the lifetime defined at the potential reaching 1.9 V and 2.0 V vs. RHE, respectively. The theoretical dissolution rate was calculated at 25 °C and applied a potential of 1.8 V vs. RHE.

PEM Water Electrolysis

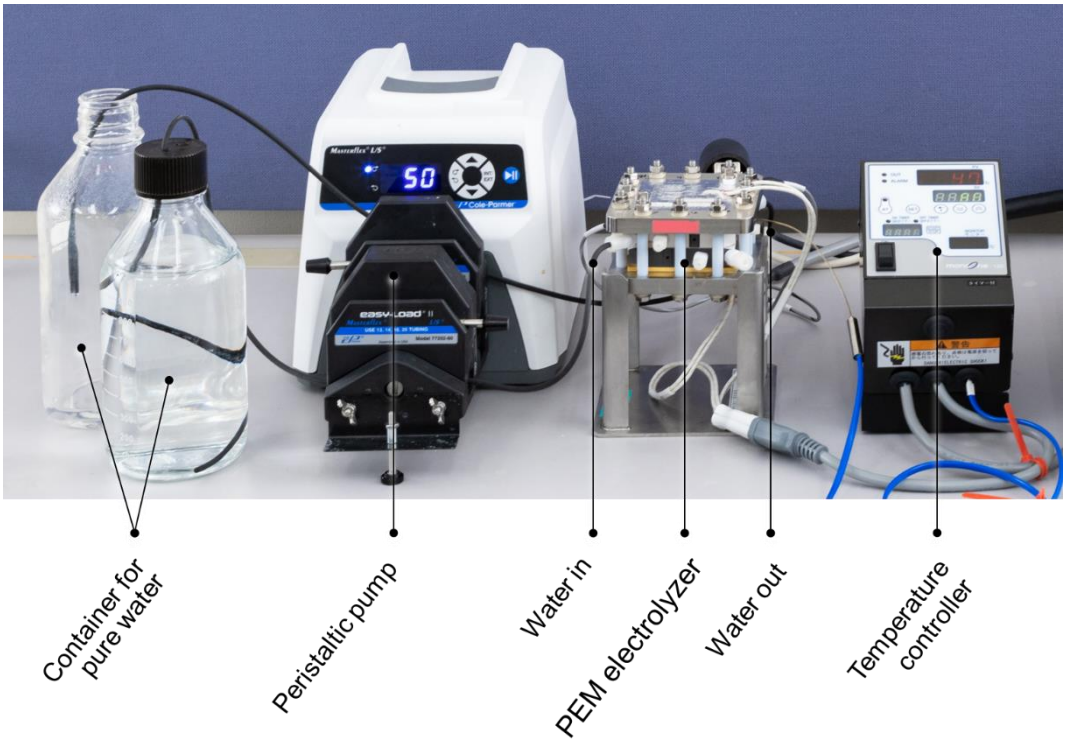

Supplementary Figure 43. Photo of the experimental setup for PEM electrolysis. Photo and description of the experimental setup for PEM water electrolysis and long-time test.

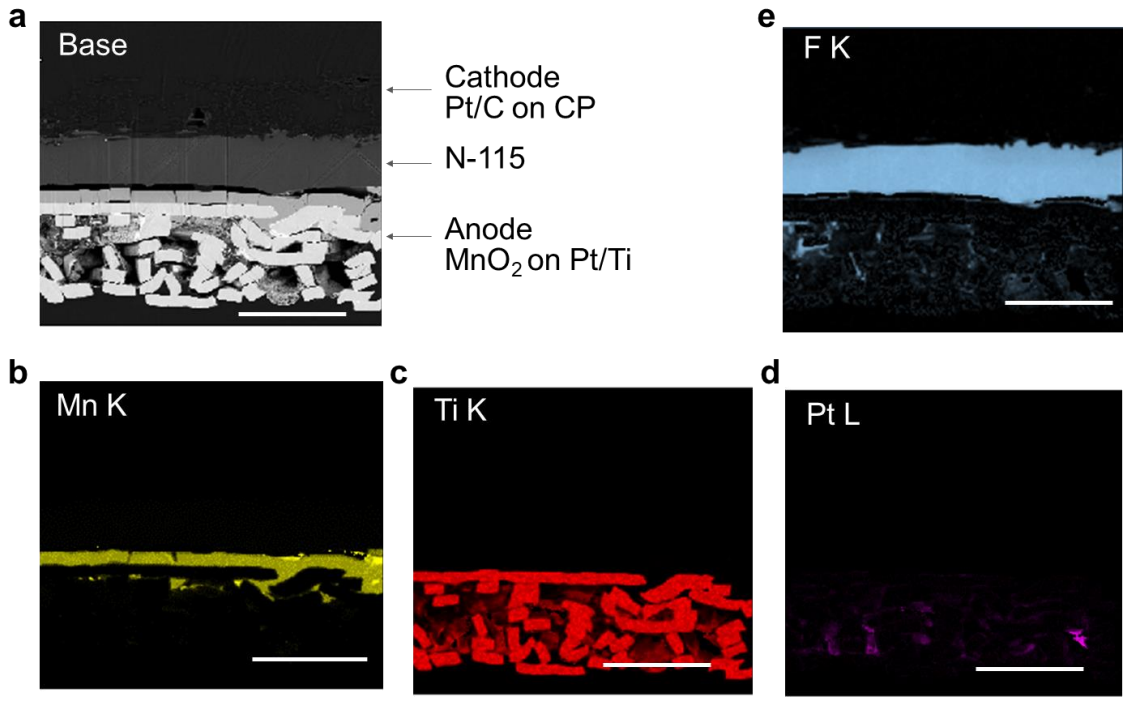

Supplementary Figure 44. Cross-section images of the MEA sample with γ-MnO_2 catalyst.
(**a**) Cross-sectional scanning electron microscopy images of a Membrane Electrode Assembly (MEA) with γ-MnO_2 catalyst as the anode. Energy dispersive X-ray (EDX) mapping analysis of Mn (**b**), Ti (**c**), Pt (**d**), and F (**e**) represent the γ-MnO_2 catalyst, Pt/Ti mesh and Nafion 115 membrane (including the Nafion ionomer added for MEA preparation), respectively. Scale bar, 250 μm.

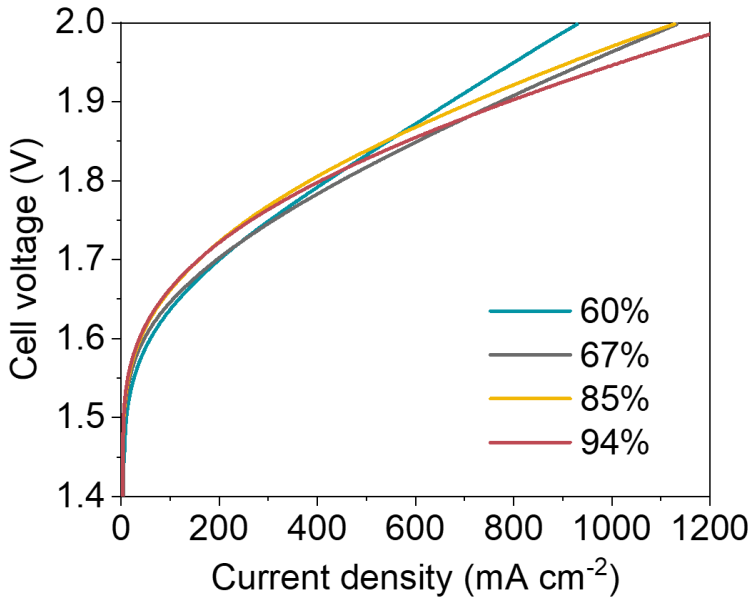

Supplementary Figure 45. Polarization curves of γ-MnO_2 MEAs measured in PEM. Polarization curves of γ-MnO_2 MEAs measured in PEM setup at 80 °C. All the MEAs were fabricated with Nafion 115 membrane.

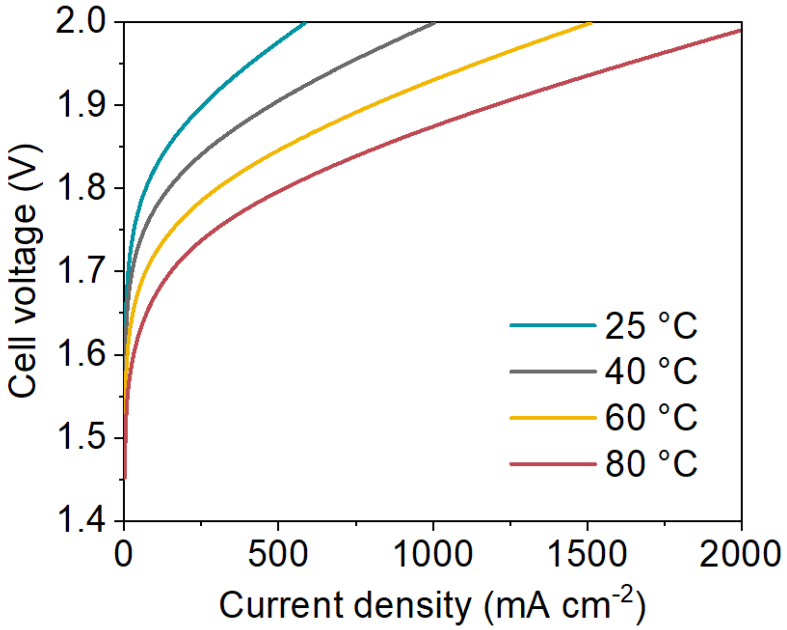

Supplementary Figure 46. Polarization curves of γ-MnO_2 MEAs at different temperature.
Polarization curves of γ-MnO_2 MEAs measured in PEM setup at 25, 40, 60, and 80 °C. All the MEAs were fabricated with Nafion 115 membrane.

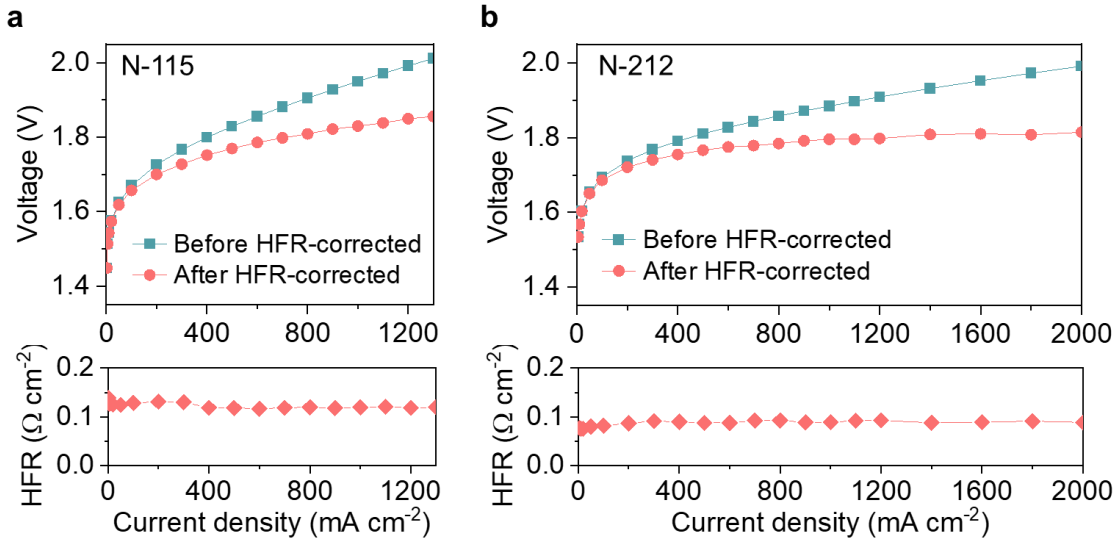

Supplementary Figure 47. Polarization curves of M94% MEA fabricated with Nafion 115 and Nafion 212.

(**a**) Polarization curves of M94% MEA fabricated with Nafion 115 (N-115) membrane and the corresponding high-frequency resistance (HFR) values. (**b**) Polarization curves of M94% MEA fabricated with Nafion 212 (N-212) membrane and the corresponding HFR values. All the PEM measurements were performed at atmospheric pressure and 80 °C.

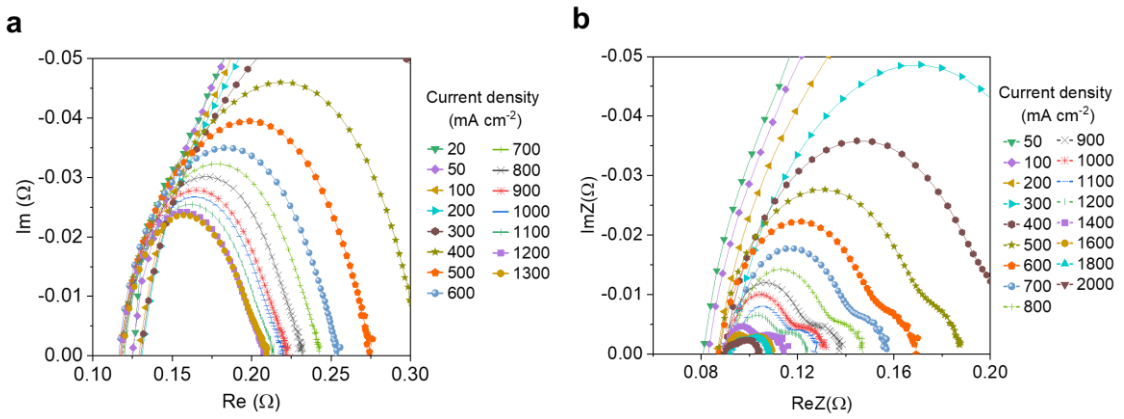

Supplementary Figure 48. Nyquist plot of the Galvanostatic impedance measurements.

(**a**) Nyquist plot of the Galvanostatic impedance measurements for M94% MEA fabricated with Nafion 115 membrane. (**b**) Nyquist plot of the Galvanostatic impedance measurements for M94% MEA fabricated with Nafion 212 membrane.

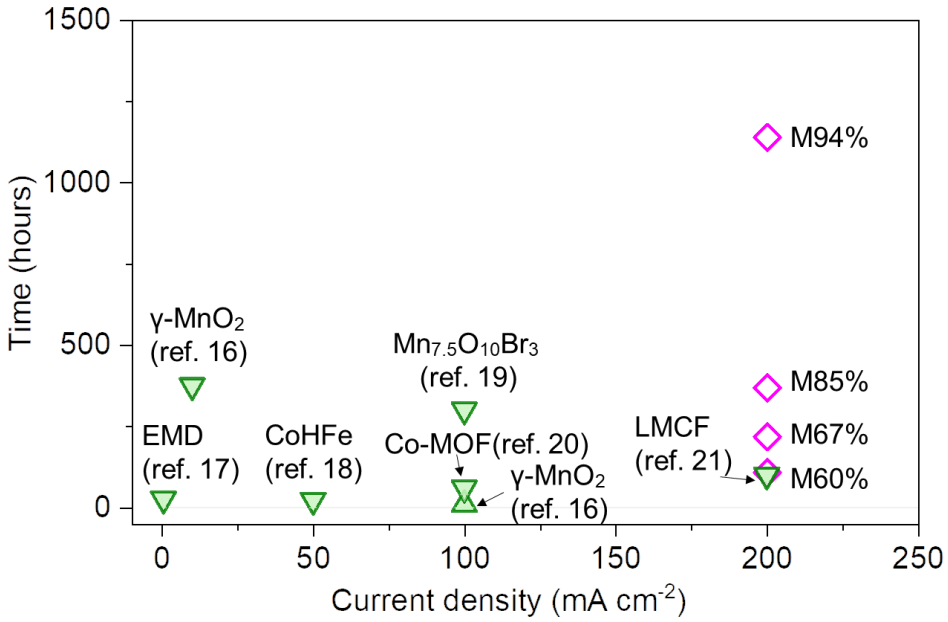

Supplementary Figure 49. Stability comparison of γ-MnO_2 with other earth-abundant OER catalysts reported in the literature.
Stability of the synthesized γ-MnO_2 catalysts in PEM electrolyzer and comparison with other earth-abundant OER catalysts reported in the literature[16-21]. Upward and downward triangles represent lifetime and operation time, respectively. The stability of LMCF[21] was measured with Nafion 212 membrane at an cell voltage of 1.65 V (current density ~ 200 mA cm^{-2}). The lifetime of γ-MnO_2 was defined at the cell voltage reaching 2.0 V.

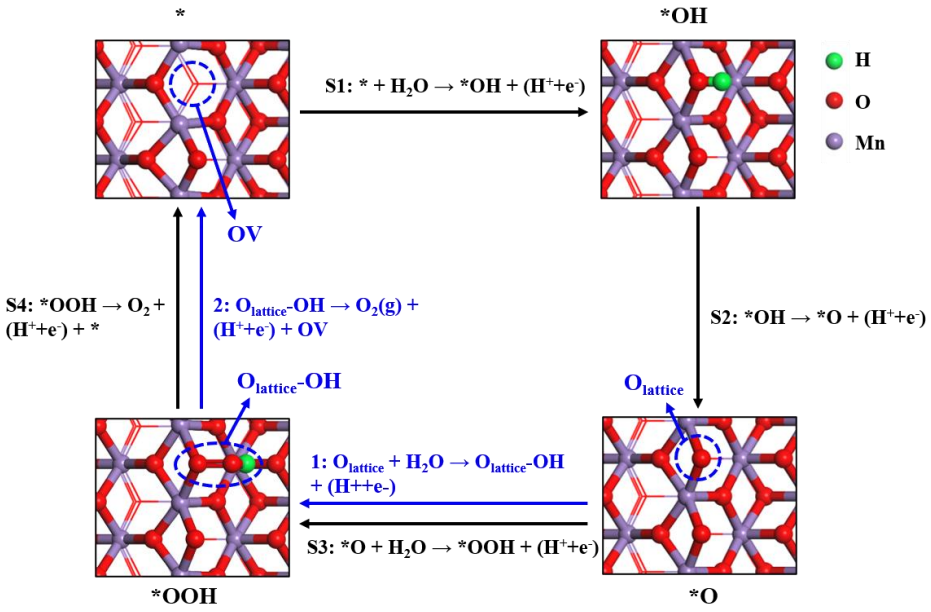

Supplementary Figure 50. Scheme illustration of OER and lattice O dissolution. Elementary steps of adsorbate evolution mechanism (AEM) of OER on the OV site of γ-MnO_2 (black arrows and labels) and $O_{lattice}$ dissolution (blue arrows and labels). The detail explanation can be found in Supplementary Note 3.

Supplementary Tables

Supplementary Table 1. PDF fitting results for the four γ-MnO_2 samples.

PDF fitting results for the four γ-MnO_2 samples. The detail fitting procedure can be found in the Supplementary Note 2. R_w was shown to validate the rational fitting.

Samples	M94%		M85%		M67%		M60%	
Phase	β-MnO_2	R-MnO_2[c]	β-MnO_2	R-MnO_2	β-MnO_2	R-MnO_2	β-MnO_2	R-MnO_2
Scale	0.300(6)	0.034(4)	0.268(6)	0.131(5)	0.131(4)	0.282(7)	0.079(4)	0.358(8)
a / Å	4.4059(6)	4.385(2)	4.407(1)	4.385(2)	4.404(2)	4.359(3)	4.409(4)	4.385(2)
b / Å	4.4059(6)	9.495(5)	4.407(1)	9.495(5)	4.404(2)	9.470(6)	4.409(4)	9.495(5)
c / Å	2.8671(7)	2.826(2)	2.865(1)	2.826(2)	2.862(3)	2.845(2)	2.866(5)	2.826(2)
U_{iso} (Mn)	0.0038(1)	0.0038(1)	0.0045(1)	0.0045(1)	0.0044(2)	0.0044(2)	0.0053(2)	0.0053(2)
U_{iso} (O)	0.024(1)	0.024(1)	0.035(2)	0.035(2)	0.017(2)	0.017(2)	0.014(1)	0.014(1)
Mn[a]	*x* = 0 *y* = 0 *z* = 0	*x* = 0.006(1) *y*= 0.1314(2) *z* = 1/4	*x* = 0 *y* = 0 *z* = 0	*x* = 0.006(1) *y* = 0.1314(2) *z* = 1/4	*x* = 0 *y* = 0 *z* = 0	*x* = 0.003(2) *y*=0.1311(3) *z* = 1/4	*x* = 0 *y* = 0 *z* = 0	*x* = 0.006(1) *y*=0.1314(2) *z* = 1/4
O[a] (1)	*x* = 0.305(1) *y* = 0.305(1) *z* = 0	*x* = 0.282(2) *y* = 0.293(1) *z* = 1/4	*x* = 0.302(2) *y* = 0.302(2) *z* = 0	*x* = 0.282(2) *y* = 0.293(1) *z* = 1/4	*x* = 0.323(2) y= 0.323(2) z = 0	*x* = 0.270(4) *y* = 0.292(2) *z* = 1/4	*x* = 0.326(3) *y* = 0.326(3) *z* = 0	*x* = 0.282(2) *y* = 0.293(1) *z* = 1/4
O[a] (2)		*x* = 0.730(2) *y* = 0.468(1) *z* = 1/4		*x* = 0.730(2) *y* = 0.468(1) *z* = 1/4		*x* = 0.726(3) *y* = 0.467(1) *z* = 1/4		*x* = 0.730(2) *y* = 0.468(1) *z* = 1/4
Mn-O_{pla} length[b] / Å	1.886(3)	1.894(5)	1.888(9)	1.894(5)	1.874(8)	1.901(4)	1.875(8)	1.894(5)
Mn-O_{pxr} length[b] / Å		1.930(1)		1.930(1)		1.920(7)		1.930(1)
R_w	0.22		0.28		0.30		0.28	

[a]Only *x*, *y* and *z* of symmetrically independent atoms are provided. The fractional coordinates of the atoms at special positions were fixed according to the symmetry of the space.

[b]The bond length was calculated by averaging the bonding between oxygen and three neighbors Mn atoms.

[c]The lattice parameters and atom coordinates of the R-MnO_2 phase in both M94% and M85% were fixed the same as the values of M60% as the ratio of R-MnO_2 phase was low.

Supplementary Table 2. Fitting parameters of Mn K-edge EXAFS spectra of standard β-MnO_2 sample.

Fitting parameters of the Fourier-transformed k^3-weighted Mn K-edge EXAFS spectra of standard β-MnO_2 sample. The standard deviations are shown in parentheses. Two commonly used parameters, *R*-factor and reduced chi-square, are shown to validate the rational fitting.

Path	N[a]	R (Å)	σ^2 (Å^2)	S_0^2	ΔE_0 (eV)	Reduced chi-square	***R***-factor[b]
Mn-O	6	1.882 (0.005)	0.0028 (0.0005)				
Mn-Mn.1 (second shell)	2	2.881 (0.007)	0.0021 (0.0006)	0.78 (0.06)	-1.0 (0.9)	363	0.021
Mn-Mn.2 (third shell)	8	3.438 (0.006)	0.0041 (0.0005)				

[a]The coordination numbers for all of the paths were fixed to the crystallography values.
[b]The definition of *R*-factor is:

$$R\text{ factor} = \frac{\Sigma_i k^3\left(\chi_i^{\text{data}}(k) - \chi_i^{\text{fit}}(k)\right)^2}{\Sigma_i\left(k^3\chi_i^{\text{data}}(k)\right)^2} \quad (1)$$

Supplementary Table 3. Fitting parameters of Mn K-edge EXAFS spectra of M94%. Fitting parameters of the Fourier-transformed k^3-weighted Mn K-edge EXAFS spectra of M94%. The standard deviations are shown in parentheses. Two commonly used parameters, *R*-factor and reduced chi-square, are shown to validate the rational fitting.

Path	*N*	*R* (Å)	σ^2 (Å^2)	Reduced chi-square	***R***-factor[b]
Mn-O	6[a]	1.882 (0.003)	0.0039 (0.0003)		
Mn-Mn.1 (second shell)	1.7 (0.4)	2.871 (0.006)	0.003 (0.001)	493	0.017
Mn-Mn.2 (third shell)	5.4 (0.7)	3.434 (0.003)	0.0033 (0.0007)		

[a]Mn-O coordination number was fixed at 6.
[b]Supplementary Equation 1

Supplementary Table 4. Fitting parameters of Mn K-edge EXAFS spectra of M85%. Fitting parameters of the Fourier-transformed k^3-weighted Mn K-edge EXAFS spectra of M85%. The standard deviations are shown in parentheses. Two commonly used parameters, *R*-factor and reduced chi-square, are shown to validate the rational fitting.

Path	*N*	*R* (Å)	σ^2 (Å^2)	Reduced chi-square	***R***-factor[b]
Mn-O	6[a]	1.886 (0.004)	0.0041 (0.0004)		
Mn-Mn.1 (second shell)	2.0 (0.5)	2.871 (0.006)	0.003 (0.001)	761	0.022
Mn-Mn.2 (third shell)	4.7 (0.8)	3.433 (0.004)	0.0033 (0.0008)		

[a]Mn-O coordination number was fixed at 6.
[b]Supplementary Equation 1

Supplementary Table 5. Fitting parameters of Mn K-edge EXAFS spectra of M67%. Fitting parameters of the Fourier-transformed k^3-weighted Mn K-edge EXAFS spectra of M67%. The standard deviations are shown in parentheses. Two commonly used parameters, *R*-factor and reduced chi-square, are shown to validate the rational fitting.

Path	*N*	*R* (Å)	σ^2 (Å^2)	Reduced chi-square	***R***-factor[b]
Mn-O	6[a]	1.889 (0.003)	0.0042 (0.0003)	439	0.016
Mn-Mn.1 (second shell)	2.4 (0.4)	2.870 (0.005)	0.0039 (0.0009)		
Mn-Mn.2 (third shell)	3.8 (0.7)	3.434 (0.004)	0.0035 (0.0008)		

[a]Mn-O coordination number was fixed at 6.
[b]Supplementary Equation 1

Supplementary Table 6. Fitting parameters of Mn K-edge EXAFS spectra of M60%. Fitting parameters of the Fourier-transformed k^3-weighted Mn K-edge EXAFS spectra of M60%. The standard deviations are shown in parentheses. Two commonly used parameters, *R*-factor and reduced chi-square, are shown to validate the rational fitting.

Path	*N*	*R* (Å)	σ^2 (Å^2)	Reduced chi-square	***R***-factor[b]
Mn-O	6[a]	1.892 (0.003)	0.0040 (0.0003)		
Mn-Mn.1 (second shell)	2.9 (0.5)	2.872 (0.005)	0.005 (0.001)	463	0.019
Mn-Mn.2 (third shell)	3.2 (0.7)	3.440 (0.005)	0.004 (0.001)		

[a]Mn-O coordination number was fixed at 6.
[b]Supplementary Equation 1

Supplementary Table 7. Fitting parameters of XPS Mn2*p* spectrum of M60%, M67%, M85% and M94%.

No	Name	Position (eV)	FWHM (eV)	Line shape	%At			
					M60%	M67%	M85%	M94%
1	Mn^{4+}-Peak 1	642.0	0.90	GL(50)	26.8	26.9	27.1	27.8
2	Mn^{4+}-Peak 2	642.8	0.90	GL(50)	14.3	14.4	14.5	14.9
3	Mn^{4+}-Peak 3	643.4	0.90	GL(50)	13.3	13.4	13.4	13.8
4	Mn^{4+}-Peak 4	644.1	0.90	GL(50)	7.4	7.5	7.5	7.7
5	Mn^{4+}-Peak 5	644.9	0.90	GL(50)	4.5	4.5	4.5	4.7
6	Mn^{4+}-Peak 6	645.8	0.90	GL(50)	2.3	2.3	2.4	2.4
7	Mn^{4+}-Peak 7	646.9	0.90	GL(50)	1.0	1.0	1.0	1.0
8	Mn^{4+}-Peak 8	647.1	0.90	GL(50)	0.4	0.4	0.4	0.4
9	Mn^{3+}-Peak 1	640.8	1.05	GL(50)	7.3	7.1	7.0	6.4
10	Mn^{3+}-Peak 2	641.6	1.05	GL(50)	7.3	7.2	7.0	6.5
11	Mn^{3+}-Peak 3	642.3	1.05	GL(50)	5.8	5.7	5.6	5.2
12	Mn^{3+}-Peak 4	643.0	1.05	GL(50)	4.5	4.4	4.3	4.0
13	Mn^{3+}-Peak 5	643.8	1.05	GL(50)	2.4	2.3	2.3	2.1
14	Mn^{3+}-Peak 6	644.7	1.05	GL(50)	1.3	1.3	1.2	1.1
15	Mn^{3+}-Peak 7	645.7	1.05	GL(50)	0.5	0.5	0.5	0.5
16	Mn^{3+}-Peak 8	639.0	1.37	GL(50)	0.3	0.3	0.3	0.2
17	Mn^{2+}-Peak 1	639.3	1.15	GL(50)	0.2	0.3	0.4	0.4
18	Mn^{2+}-Peak 2	640.3	1.15	GL(30)	0.2	0.2	0.3	0.3
19	Mn^{2+}-Peak 3	641.1	1.15	GL(30)	0.1	0.2	0.2	0.2
20	Mn^{2+}-Peak 4	642.0	1.15	GL(30)	0.1	0.1	0.1	0.2
21	Mn^{2+}-Peak 5	643.0	1.15	GL(30)	0.0	0.1	0.1	0.1
22	Mn^{2+}-Peak 6	644.1	1.55	GL(30)	0.0	0.0	0.0	0.0
23	Mn^{2+}-Peak 7	646.2	2.57	GL(30)	0.1	0.1	0.1	0.1
24	Mn^{2+}-Peak 8	637.6	1.35	GL(30)	0.0	0.0	0.0	0.0

Supplementary Table 8. Solvation energies calculated with explicit and implicit methods.

Species	Solvation energies (eV)			
	Explicit model a[#]	Explicit model b	Implicit model (VASPsol)	Average
*OH	-0.14	-0.12	-0.06	-0.11
*O	-0.09	-0.11	-0.08	-0.09
*OOH	-0.04	-0.06	-0.06	-0.05

[#]The structures of explicit model a and b are presented in Supplementary Figure 23.

Supplementary Table 9. PDF fitting results for M60% and M94% after electrolysis.

PDF fitting results for the M60% and M94% after electrolysis for 40 h at 200 mA cm^{-2}_{geo}. The detailed fitting procedure can be found in the Supplementary Note 2. R_w was shown to validate the rational fitting.

Samples	**M94%-after**		**M60%-after**	
Phase	β-MnO_2	R-MnO_2[c]	β-MnO_2	R-MnO_2
Scale	0.248(6)	0.041(5)	0.047(4)	0.187(7)
***a* / Å**	4.407(9)	4.385(2)	4.441(7)	4.388(4)
***b* / Å**	4.407(9)	9.495(5)	4.441(7)	9.56(1)
***c* / Å**	2.866(1)	2.826(2)	2.841(8)	2.808(4)
U_{iso} (Mn)	0.004(1)	0.004(1)	0.006 (7)	0.006 (7)
U_{iso} (O)	0.027(2)	0.027(2)	0.011(2)	0.011(2)
Mn[a]	*x* = 0 *y* = 0 *z* = 0	*x* = 0.006(1) *y* = 0.131 (4) *z* = 1/4	*x* = 0 *y* = 0 *z* = 0	*x* = 0.002(3) *y* =0.131 (5) *z* = ¼
O[a] (1)	*x* = 0.303(2) *y* = 0.303(2) *z* = 0	*x* = 0.282(2) *y* = 0.293(1) *z* = 1/4	*x* = 0.324(4) *y* = 0.324(4) *z* = 0	*x* = 0.273(5) *y* = 0.296(2) *z* = ¼
O[a] (2)		*x* = 0.730(2) *y* = 0.468(1) *z* = 1/4		*x* = 0.724(4) *y* = 0.468(2) *z* = ¼
Mn-O_{pla} length[b] / Å	1.887(5)	1.892(3)	1.878(2)	1.895(3)
Mn-O_{pyr} length[b] / Å		1.930(1)		1.917(7)
R_w	0.25		0.34	

Supplementary Table 10. Fitting parameters of Mn K-edge EXAFS spectra of M94% after electrolysis.

Fitting parameters of the Fourier-transformed k^3-weighted Mn K-edge EXAFS spectra of M94%-40h. The standard deviations are shown in parentheses. Two commonly used parameters, *R*-factor and reduced chi-square, are shown to validate the rational fitting.

Path	*N*	*R* (Å)	σ^2 (Å^2)	Reduced chi-square	***R***-factor[b]
Mn-O	6[a]	1.887 (0.004)	0.0041 (0.0004)		
Mn-Mn.1 (second shell)	1.6 (0.4)	2.878 (0.008)	0.003 (0.001)	621	0.031
Mn-Mn.2 (third shell)	4.8 (0.4)	3.434 (0.004)	0.0031 (0.0006)		

[a]Mn-O coordination number was fixed at 6.
[b]Supplementary Equation 1

Supplementary Table 11. Fitting parameters of Mn K-edge EXAFS spectra of M60% after electrolysis.

Fitting parameters of the Fourier-transformed k^3-weighted Mn K-edge EXAFS spectra of M60%-40h. The standard deviations are shown in parentheses. Two commonly used parameters, *R*-factor and reduced chi-square, are shown to validate the rational fitting.

Path	*N*	*R* (Å)	σ^2 (Å^2)	Reduced chi-square	***R***-factor[b]
Mn-O	6[a]	1.893 (0.004)	0.0049 (0.0004)		
Mn-Mn.1 (second shell)	2.6 (0.4)	2.870 (0.007)	0.006 (0.001)	537	0.028
Mn-Mn.2 (third shell)	2.9 (0.8)	3.441 (0.007)	0.004 (0.001)		

[a]Mn-O coordination number was fixed at 6.
[b]Supplementary Equation 1

Supplementary Table 12. Elementary steps in the O_{pyr} and O_{pla} mechanisms for catalyst dissolution.

Elementary steps in the O_{pyr} and O_{pla} mechanisms for catalyst dissolution and calculated reaction free energies.

	Steps	Δ*G* (eV)			
		M50%	**M60%**	**M67%**	**M80%**
O_{pyr} mechanism	$O_{t1} \rightarrow O_{t1}$-OH	1.47	1.47	1.59	1.49
	O_{t1}-OH $\rightarrow O_{t1}V$	1.27	1.15	1.16	1.04
	$Mn_1 \rightarrow Mn_1V$	1.38	1.15	1.37	1.45
	$O_{pyr} \rightarrow O_{pyr}$-OH[#]	**1.90**	**1.92**	**1.89**	**1.91**
	O_{pyr}-OH $\rightarrow O_{pyr}V$	0.87	0.96	0.90	0.60

	Steps	Δ*G* (eV)			
		M60%	**M67%**	**M80%**	**M100%**
O_{pla} mechanism	$O_{t2} \rightarrow O_{t2}$-OH	1.54	1.36	1.55	1.54
	O_{t2}-OH $\rightarrow O_{t2}V$	1.36	1.22	1.11	1.05
	$Mn_2 \rightarrow Mn_2V$	1.31	1.27	1.38	1.32
	$O_{pla} \rightarrow O_{pla}$-OH[#]	**2.16**	**2.15**	**2.14**	**2.10**
	O_{pla}-OH $\rightarrow O_{pla}V$	1.28	0.47	-0.35	-0.41

[#]Potential-determining step

Supplementary Table 13. Data and references for Fig. 3b in the main text.

Number in Fig. 3b	Catalyst	Electrolyte[a]	Stability[b]	Ref.
1	Amorphous $CoFeO_x$	pH 2 in Pi	2 h at 1 mA cm^{-2}_{geo} (LT)	22
2	Amorphous $CoPbO_x$	pH 2.5 in Pi	8 h at 1 mA cm^{-2}_{geo} (LT)	22
3	Amorphous $CoFePbO_x$	pH 2 in Pi	50 h at 1 mA cm^{-2}_{geo} (OT)	22
4	Ti-MnO_2	0.5 M H_2SO_4	2 h at 1.9 V vs. RHE (OT), j from 7.2 to 6 mA cm^{-2}_{geo}	23
5	$Cu_{1.5}Mn_{1.5}O_4$	0.5 M H_2SO_4	20 h at 1.55 V vs. RHE (OT), j from ~10 to 1.5 mA cm^{-2}_{geo}	24
6	1T-MoS_2	pH 0.3 H_2SO_4	2 h at 10 mA cm^{-2}_{geo} (OT)	25
7	Mn-doped $FeP/Co_3(PO_4)_2$	0.5 M H_2SO_4	8.3 h at 5 mA cm^{-2}_{geo} (OT)	26
8	Co_2TiO_4	0.5 M H_2SO_4	10 h at 1.79 V vs. RHE (OT) j from 10 to 5 mA cm^{-2}_{geo}	27
9	Crystalline Co_3O_4	0.5 M H_2SO_4	15 h at 10 mA cm^{-2}_{geo} (LT)	28
10	R20-Mn	0.5 M H_2SO_4	20 h at 10 mA cm^{-2}_{geo} (OT)	29
11	c-Fe_2O_3	pH 0.3 H_2SO_4	24 h at 10 mA cm^{-2}_{geo} (OT)	30
12	NiFeP	0.05 M H_2SO_4	30 h at 10 mA cm^{-2}_{geo} (OT)	31
13	Ni42 steel	pH 1 H_2SO_4	42 h at 10 mA cm^{-2}_{geo} (OT)	32
14	Co_3O_4@C	1 M H_2SO_4 (pH 0.1)	40 h at 10 mA cm^{-2}_{geo} (OT)	33
15	$Co_{0.05}Fe_{0.96}O_y$	pH 0.3 H_2SO_4	50 h at 10 mA cm^{-2} (LT)	34
16	Ni_2Ta	0.5 M H_2SO_4	66 h at 10 mA cm^{-2}_{geo} (OT) FE ~ 85%	35
17	Co_3O_4/CeO_2	0.05M H_2SO_4	100 h at 10 mA cm^{-2}_{geo} (OT)	36
18	$Ni_{0.5}Mn_{0.5}Sb_{1.7}O_y$	1.0 M H_2SO_4	168 h at 10 mA cm^{-2}_{geo} (OT)	37
19	$Mn_{7.5}O_{10}Br_3$	0.5 M H_2SO_4	500 h at 10 mA cm^{-2}_{geo} (OT)	19

20	γ-MnO_2	pH 2 H_2SO_4 with 0.5 M Na_2SO_4	8000 h at 10 mA cm^{-2}_{geo} (OT)	16
21	F-$Cu_{1.5}Mn_{1.5}O_4$	pH 0.3 H_2SO_4	24 h at 16 mA cm^{-2}_{geo} (OT)	38
22	FeN_4/NF/EG	0.5 M H_2SO_4	24 h at 20 mA cm^{-2}_{geo} (OT)	39
23	$Mn_xSb_{1-x}O_z$	1 M H_2SO_4	2 h at 10 mA cm^{-2}_{geo} (OT)	40
24	$CoFePbO_x$	1 M H_2SO_4	13 h at 100 mA cm^{-2}_{geo} (OT)	41
25	$CoFePbO_x$	1 M H_2SO_4	7 h at 500 mA cm^{-2}_{geo} (OT)	41
26	Co_3O_4/C	0.5 M H_2SO_4	86.8 h at 100 mA cm^{-2}_{geo} (LT)	42
27	Co_3O_4	pH 1 H_2SO_4	7 h at 100 mA cm^{-2}_{geo} (LT)	43
28	γ-MnO_2	pH 1 H_2SO_4	33 h at 100 mA cm^{-2} (LT)	43
29	Co_2MnO_4/FTO	pH 1 H_2SO_4	326 h at 100 mA cm^{-2}_{geo} (LT)	43
30	Co_2MnO_4/FTO	pH 1 Pi	1440 h at 100 mA cm^{-2}_{geo} (LT)	43
31	Co_2MnO_4/PtTi mesh	pH 1 Pi	1500 h at 200 mA cm^{-2}_{geo} (LT)	43
32	Co_2MnO_4/FTO	pH 1 Pi	220 h at 200 mA cm^{-2}_{geo} (LT)	43
33	Co_2MnO_4/FTO	pH 1 H_2SO_4	56 h at 200 mA cm^{-2}_{geo} (LT)	43
34	Co_2MnO_4/FTO	pH 1 Pi	72 h at 500 mA cm^{-2}_{geo} (LT)	43
35	Co_2MnO_4/FTO	pH 1 H_2SO_4	20 h at 500 mA cm^{-2}_{geo} (LT)	43
36	Co_2MnO_4/FTO	pH 1 Pi	7.5 h at 1000 mA cm^{-2}_{geo} (LT)	43
37	Co_2MnO_4/FTO	pH 1 H_2SO_4	2.8 h at 1000 mA cm^{-2}_{geo} (LT)	43

[a]Pi: phosphate additive.
[b]The reported stability is shown as either operation time (OT, time length of electrolysis) or lifetime (LT, time until deactivation).

Supplementary Notes

Supplementary Note 1. The pair distribution function.

The pair distribution function (PDF), gives the weighted probability of detecting any pair of atoms separated by a distance *r*. The pair distribution function $g(r)$ is defined as:

$$g(r) = \frac{1}{4\pi\rho_0 r^2 N}\sum_i \sum_{j\neq i} \delta(r - r_{ij}) \quad (2)$$

where ρ_0 is the average number density of atoms, N is the total number of atom, r_{ij} refers to the distance between the ith and jth atoms in the system containing N atoms, and δ is the Dirac delta function whose integral equals to one only when $r = r_{ij}$. In practice, the reduced atomic pair distribution function $G(r)$ is used more frequently:

$$G(r) = 4\pi r\rho_0[g(r) - 1] \quad (3)$$

$G(r)$ can be calculated directly from the measured total scattering function $S(Q)$ through the Fourier transform:

$$G(r) = \frac{2}{\pi}\int_0^\infty Q[S(Q) - 1]\sin(Qr)\,\mathrm{d}Q \quad (4)$$

where Q is the amplitude of transferred momentum calculated by the difference between scattered and incident wavevectors. $S(Q)$ can be calculated from the measured coherent scattering intensity $I_{\mathrm{coh}}(Q)$:

$$S(Q) = 1 + \frac{I^{coh}(Q) - \sum c_i |f^i(Q)|^2}{|\sum c_i f^i(Q)|^2} \quad (5)$$

where c_i is the atomic concentration of the ith type of element and $f^i(Q)$ is its atomic X-ray scattering factor or neutron scattering length. The coherent scattering intensity $I_{\mathrm{coh}}(Q)$ can be directly collected from the experimentally measured total intensity $I(Q)$ when properly corrected for factors such as incoherent intensity, background noises, detector efficiency, and multiple scattering.

Bond lengths are commonly determined directly from the peak position. The coordination number of an atom-atom correlation, or the number of neighbors at a specific distance, can be obtained from the integrated intensity under a PDF peak. Additionally, information about the static and dynamic disorder of atoms involved in the pair can be revealed by the width of PDF peaks.

The real-space Rietveld method is a powerful and widely used technique for obtaining a quantitative solution of the local structure from the $G(r)$ pattern. This method is similar to the well-established Rietveld analysis in diffraction-based crystallography. However, the conventional Rietveld method only refines the Bragg peaks and arbitrarily treats the diffusion signals as background, resulting in an average structure of a given model. In contrast, the real-space PDF Rietveld refinement deals with total scatterings (both diffraction and diffusion), which contains local disorders deviating from the average structure. Popular programs for performing real-space Rietveld refinement include

PDFgui[44] and DiffPy-CMI[45]. A structural model is built with a unit cell containing fraction-coordinated atoms, and then the structural parameters are refined using a least-square method for the best $G(r)$ description. For more details regarding the PDF analysis, please refer to the original book by Egami et al.[4] and the review paper by Zhu, H. et al.[3].

Supplementary Note 2. The refinement of pair distribution function.

The model of γ-MnO_2 was constructed following a procedure described in the literature[46,47], where it was shown that $G(r)$ of γ-MnO_2 can be described by the weighted sum of ramsdellite (R-MnO_2, space group *Pbnm*) and pyrolusite (β-MnO_2, space group $P4_2/mnm$). Refinements were carried out in the range of 1.0–20.0 Å in 0.01 Å steps. The values of the instrument parameters Q_{damp} and Q_{broad} for γ-MnO_2 were fixed to those derived from the fitting of the pure β-MnO_2 standard sample. Refinement of the parameters for γ-MnO_2 was conducted using the following procedural steps. 1. The scale factors of β-MnO_2 and R-MnO_2 phase in M94% were refined. 2. The cell parameters of the β-MnO_2 phase were refined while those of R-MnO_2 were fixed, as the percentage of the R-MnO_2 phase was low. 3. The atomic coordinates of the β-MnO_2 phase were refined with the appropriate constraints considering the symmetry of the phase. 4. The isotropic atomic displacement parameters (ADPs) of Mn and O atoms were refined. 5. The linear atomic correlation factor *delta1* was refined. The isotropic ADPs and *delta1* were constrained to have the same value for the β-MnO_2 and R-MnO_2 phases. 6. The particle size effect parameter *spdiameter* was refined. The same value of *spdiameter* was used for the β-MnO_2 and R-MnO_2 phases. 7. All of the above procedures were initially repeated sequentially, and were then gradually conducted simultaneously to avoid falling into false local minima. 8. The result of M94% after the refinement was employed as the initial model for M85%. A similar procedure was performed for M85%. 9. The result of M85% was used as the initial model for M67%, and that of M67% was used for M60%. The structure parameters of the R-MnO_2 phase in M67% and M60% were also refined. 10. The structural parameters of the R-MnO_2 phase in M60% were used for the re-refinement of the other samples and for updating the structure models of the R-MnO_2 phase. 11. All of the parameters were carefully examined to determine whether they were chemically and physically plausible. Refinement parameters for the γ-MnO_2 samples are provided in Supplementary Table 1.

Supplementary Note 3. Validation of Eqs. 4 and 5 in the main manuscript.

To validate Eq. 5, we assumed a typical adsorbate evolution mechanism (AEM) of OER on the OV site of γ-MnO_2, as illustrated in Supplementary Figure 50 (the black arrows and labels). The elementary steps of AEM can be written as:

$$* + H_2O \rightarrow *OH + (H^+ + e^-) \quad (6)$$

$$*OH \rightarrow *O + (H^+ + e^-) \quad (7)$$

$$*O + H_2O \rightarrow *OOH + (H^+ + e^-) \quad (8)$$

$$*OOH \rightarrow O_2(g) + (H^+ + e^-) + * \quad (9)$$

To calculate the reaction free energies of Supplementary Equations 6-9, we need calculate the adsorption free energies of *O [G(*O)], *OH [G(*OH)], and *OOH [G(*OOH)] at first, with reference to the energy of gas-phase H_2O at 0.035 bar and H_2. Note that, the gas-phase H_2O at a pressure of 0.035 bar is in equilibrium with liquid H_2O at 298.15 K, i.e., the chemical potentials of them are equal. Hence the gas-phase H_2O at 0.035 bar can be used as the reference. Then the reaction free energies of Supplementary Equations 6-9 at 0 V vs. RHE can be calculated via the following equations, based on the well-known computational hydrogen electrode (CHE) model[48].

$$\Delta G_6 = G(*OH) \quad (10)$$

$$\Delta G_7 = G(*O) - G(*OH) \quad (11)$$

$$\Delta G_8 = G(*OOH) - G(*O) \quad (12)$$

$$\Delta G_9 = 4.92\ [eV] - G(*OOH) \quad (13)$$

Here, the total energy difference of OER (4.92 eV), H_2O and H_2 were used as reference to calculate the ΔG_9 (Supplementary Equation 13) due to the limitations in accurately describing the high-spin ground state of O_2 molecule in DFT calculations. This method has been used widely in DFT study of OER[49,50].

For lattice O dissolution, the elementary steps of $O_{lattice}$ dissolution (Eq. 2 and Eq. 3) are equivalent to the last two steps (Supplementary Equations 8 and 9) of AEM on the OV site, as shown in Supplementary Figure 50 (the blue arrows). Hence, the reaction free energies of Eq. 2 and Eq. 3 are equal to ΔG_8 and ΔG_9, respectively, demonstrating Eq. 5 is valid.

Supplementary Note 4. Derivation of Eq. 8

Theoretically, the Gibbs free energies (G) of a system can be calculated via the following equation:

$$G = U + pV - TS \quad (14)$$

where U is the internal energy, which should include the terms of DFT energy (E^{DFT}), ZPE, and the energy of thermal contribution. The energy of thermal contribution can be calculated by integrating the heat capacity [Cp(T)] up to the relevant temperature. Thus,

$$U = E^{DFT} + ZPE + \int C_p(T)dT \quad (15)$$

The term pV is usually assumed to be negligible. In addition, the thermal contribution was also not considered in this study. In this case, the $G(Mn_{x-1}O_{2x})$ and $G(Mn_xO_{2x})$ in Eq.7 can be written as:

$$G(Mn_{x-1}O_{2x}) = E(Mn_{x-1}O_{2x})^{DFT} + ZPE(Mn_{x-1}O_{2x}) - TS(Mn_{x-1}O_{2x}) \quad (16)$$

$$G(Mn_xO_{2x}) = E(Mn_xO_{2x})^{DFT} + ZPE(Mn_xO_{2x}) - TS(Mn_xO_{2x}) \quad (17)$$

where $E(Mn_{x-1}O_{2x})^{DFT}$ and $E(Mn_xO_{2x})^{DFT}$ represent the DFT energies of $Mn_{x-1}O_{2x}$ and Mn_xO_{2x}, respectively, and ZPE and S represent zero-point energy and entropy,

respectively. Thus,

$$G(Mn_{x-1}O_{2x}) - G(Mn_xO_{2x}) = E(Mn_{x-1}O_{2x})^{DFT} - E(Mn_xO_{2x})^{DFT} + \Delta ZPE - T\Delta S \quad (18)$$

where

$$\Delta ZPE = ZPE(Mn_{x-1}O_{2x}) - ZPE(Mn_xO_{2x})$$
$$= ZPE(Mn_{x-1}O_{2x}) - [ZPE(Mn_{x-1}O_{2x}) + ZPE(Mn_{lattice})] \quad (19)$$
$$\Delta S = S(Mn_{x-1}O_{2x}) - S(Mn_xO_{2x})$$
$$= S(Mn_{x-1}O_{2x}) - [S(Mn_{x-1}O_{2x}) + S(Mn_{lattice})] \quad (20)$$

Here, we have assumed the $ZPE(Mn_xO_{2x})$ can be decomposed into $ZPE(Mn_{x-1}O_{2x})$ and $ZPE(Mn_{lattice})$, and the $S(Mn_xO_{2x})$ can be decomposed into $S(Mn_{x-1}O_{2x})$ and $S(Mn_{lattice})$. In addition, the change of ZPE and S of $Mn_{x-1}O_{2x}$ before and after reaction is assumed to be negligible. Thus,

$$\Delta ZPE = -ZPE(Mn_{lattice}) \quad (21)$$
$$\Delta S = -S(Mn_{lattice}) \quad (22)$$

Combining Eqs. 7, Supplementary Equations 18, 21, and 22, we can obtain Eq. 8. For $Mn_{lattice}$, all vibrational models were treated to estimate the entropy. The entropy contributions from these vibrational frequencies (v_i) were evaluated using the harmonic normal mode approximation as[47]:

$$S_{vib} = k_B \sum_i \left[\frac{hv_i/k_BT}{e^{hv_i/k_BT}-1} - \ln(1 - e^{-hv_i/k_BT})\right] \quad (23)$$

where k_B is Boltzmann constant, h is Planck constant, and T represents temperature.

Supplementary References

1 Chabre, Y. & Pannetier, J. Structure and electrochemical properties of the proton/γ-MnO_2 system. *Prog. Solid St. Chem.* **23**, 1-130 (1995).

2 Hill, L. I. & Verbaere, A. On the structural defects in synthetic γ-MnO_2s. *J. Solid State Chem.* **177**, 4706-4723 (2004).

3 Zhu, H. *et al.* Bridging structural inhomogeneity to functionality: Pair distribution function methods for functional materials development. *Adv. Sci.* **8**, 2003534 (2021).

4 Egami, T. & Billinge, S. J. L. *Underneath the bragg peaks: structural analysis of complex materials*. (Pergamon, 2003).

5 Hatakeyama, T., Okamoto, N. L. & Ichitsubo, T. Thermal stability of MnO_2 polymorphs. *J. Solid State Chem.* **305**, 122683 (2022).

6 Ahrens, T. J. *Mineral physics & crystallography: a handbook of physical constants*. (American Geophysical Union, 1995).

7 Biesinger, M. C. *et al.* Resolving surface chemical states in XPS analysis of first row transition metals, oxides and hydroxides: Cr, Mn, Fe, Co and Ni. *Appl. Surf. Sci.* **257**, 2717-2730 (2011).

8 Ilton, E. S., Post, J. E., Heaney, P. J., Ling, F. T. & Kerisit, S. N. XPS determination of Mn oxidation states in Mn (hydr)oxides. *Appl. Surf. Sci.* **366**, 475-485 (2016).

9 Patterson, A. The Scherrer formula for X-ray particle size determination. *Phys. Rev.* **56**, 978 (1939).

10 Petkov, V. Pair distribution functions analysis. *Mater. Charact.*, 1361-1372 (2012).

11 Mathew, K., Sundararaman, R., Letchworth-Weaver, K., Arias, T. A. & Hennig, R. G. Implicit solvation model for density-functional study of nanocrystal surfaces and reaction pathways. *J. Chem. Phys.* **140**, 084106 (2014).

12 Nakamoto, K. *Infrared and Raman spectra of inorganic and coordination compounds, part B: applications in coordination, organometallic, and bioinorganic chemistry*. (John Wiley & Sons, 2009).

13 Julien, C., Massot, M. & Poinsignon, C. Lattice vibrations of manganese oxides: Part I. Periodic structures. *Spectrochimica Acta Part A: Molecular and Biomolecular Spectroscopy* **60**, 689-700 (2004).

14 Chan, K. & Nørskov, J. K. Electrochemical Barriers Made Simple. *J. Phys. Chem. Lett.* **6**, 2663-2668 (2015).

15 Chan, K. & Nørskov, J. K. Potential dependence of electrochemical barriers from ab initio calculations. *J. Phys. Chem. Lett.* **7**, 1686-1690 (2016).

16 Li, A. *et al.* Stable potential windows for long-term electrocatalysis by manganese oxides under acidic conditions. *Angew. Chem. Int. Ed.* **58**, 5054-5058 (2019).

17 Hayashi, T., Bonnet-Mercier, N., Yamaguchi, A., Suetsugu, K. & Nakamura, R. Electrochemical characterization of manganese oxides as a water oxidation catalyst in proton exchange membrane electrolysers. *R. Soc. Open Sci.* **6**, 190122 (2019).

18 Rodríguez-García, B. *et al.* Cobalt hexacyanoferrate supported on Sb-doped SnO_2 as a non-noble catalyst for oxygen evolution in acidic medium. *Sustain. Energy Fuels* **2**, 589-597 (2018).

19 Pan, S. *et al.* Efficient and stable noble-metal-free catalyst for acidic water oxidation. *Nat. Commun.* **13**, 2294 (2022).
20 Liu, D.-J. (Invited) On the structural and mechanistic studies of PGM-free OER catalysts for PEM electrolyzer. *ECS Meeting Abstracts* **MA2022-01**, 1755-1755 (2022).
21 Chong, L. *et al.* La- and Mn-doped cobalt spinel oxygen evolution catalyst for proton exchange membrane electrolysis. *Science* **380**, 609-616 (2023).
22 Huynh, M., Ozel, T., Liu, C., Lau, E. C. & Nocera, D. G. Design of template-stabilized active and earth-abundant oxygen evolution catalysts in acid. *Chem. Sci.* **8**, 4779-4794 (2017).
23 Frydendal, R., Paoli, E. A., Chorkendorff, I., Rossmeisl, J. & Stephens, I. E. L. Toward an active and stable catalyst for oxygen evolution in acidic media: Ti-stabilized MnO_2. *Adv. Energy Mater.* **5**, 1500991 (2015).
24 Ghadge, S. D. *et al.* Influence of defects on activity-stability of $Cu_{1.5}Mn_{1.5}O_4$ for acid-mediated oxygen evolution reaction. *J. Electrochem. Soc.* **167**, 144511 (2020).
25 Wu, J. *et al.* Exfoliated 2D transition metal disulfides for enhanced electrocatalysis of oxygen evolution reaction in acidic medium. *Adv. Mater. Interfaces* **3**, 1500669 (2016).
26 Liu, H., Peng, X., Liu, X., Qi, G. & Luo, J. Porous Mn-doped $FeP/Co_3(PO_4)_2$ nanosheets as efficient electrocatalysts for overall water splitting in a wide pH range. *ChemSusChem* **12**, 1334-1341 (2019).
27 Anantharaj, S., Karthick, K. & Kundu, S. Spinel cobalt titanium binary oxide as an all-non-precious water oxidation electrocatalyst in acid. *Inorg. Chem.* **58**, 8570-8576 (2019).
28 Mondschein, J. S. *et al.* Crystalline cobalt oxide films for sustained electrocatalytic oxygen evolution under strongly acidic conditions. *Chem. Mater.* **29**, 950-957 (2017).
29 Zhao, Z. *et al.* Tailoring manganese oxide nanoplates enhances oxygen evolution catalysis in acid. *J. Catal.* **405**, 265-272 (2022).
30 Kwong, W. L., Lee, C. C., Shchukarev, A., Björn, E. & Messinger, J. High-performance iron (III) oxide electrocatalyst for water oxidation in strongly acidic media. *J. Catal.* **365**, 29-35 (2018).
31 Hu, F. *et al.* Amorphous metallic NiFeP: a conductive bulk material achieving high activity for oxygen evolution reaction in both alkaline and acidic media. *Adv. Mater.* **29**, 1606570 (2017).
32 Schäfer, H. *et al.* Steel-based electrocatalysts for efficient and durable oxygen evolution in acidic media. *Catal. Sci. Technol.* **8**, 2104-2116 (2018).
33 Yu, J. *et al.* Sustainable oxygen evolution electrocatalysis in aqueous 1 M H_2SO_4 with earth abundant nanostructured Co_3O_4. *Nat. Commun.* **13**, 4341 (2022).
34 Kwong, W. L., Lee, C. C., Shchukarev, A. & Messinger, J. Cobalt-doped hematite thin films for electrocatalytic water oxidation in highly acidic media. *Chem. Commun.* **55**, 5017-5020 (2019).
35 Mondschein, J. S. *et al.* Intermetallic Ni_2Ta electrocatalyst for the oxygen evolution reaction in highly acidic electrolytes. *Inorg. Chem.* **57**, 6010-6015 (2018).

36 Huang, J. *et al.* Modifying redox properties and local bonding of Co_3O_4 by CeO_2 enhances oxygen evolution catalysis in acid. *Nat. Commun.* **12**, 3036 (2021).
37 Moreno-Hernandez, I. A. *et al.* Crystalline nickel manganese antimonate as a stable water-oxidation catalyst in aqueous 1.0 M H_2SO_4. *Energy Environ. Sci.* **10**, 2103-2108 (2017).
38 Patel, P. P. *et al.* Noble metal-free bifunctional oxygen evolution and oxygen reduction acidic media electro-catalysts. *Sci. Rep.* **6**, 28367 (2016).
39 Lei, C. *et al.* Fe-N_4 sites embedded into carbon nanofiber integrated with electrochemically exfoliated graphene for oxygen evolution in acidic medium. *Adv. Energy Mater.* **8**, 1801912 (2018).
40 Zhou, L. *et al.* Rutile alloys in the Mn–Sb–O system stabilize Mn^{3+} to enable oxygen evolution in strong acid. *ACS Catal.* **8**, 10938-10948 (2018).
41 Chatti, M. *et al.* Intrinsically stable in situ generated electrocatalyst for long-term oxidation of acidic water at up to 80 °C. *Nat. Catal.* **2**, 457-465 (2019).
42 Yang, X. *et al.* Highly acid-durable carbon coated Co_3O_4 nanoarrays as efficient oxygen evolution electrocatalysts. *Nano Energy* **25**, 42-50 (2016).
43 Li, A. *et al.* Enhancing the stability of cobalt spinel oxide towards sustainable oxygen evolution in acid. *Nat. Catal.* **5**, 109-118 (2022).
44 Farrow, C. L. *et al.* PDFfit2 and PDFgui: computer programs for studying nanostructure in crystals. *J. Condens. Matter Phys.* **19**, 335219 (2007).
45 Juhás, P., Farrow, C. L., Yang, X., Knox, K. R. & Billinge, S. J. Complex modeling: a strategy and software program for combining multiple information sources to solve ill posed structure and nanostructure inverse problems. *Acta Crystallogr. A: Found. Adv.* **71**, 562-568 (2015).
46 Galliez, K. *et al.* Modelling and quantification of intergrowth in γ-MnO_2 by laboratory pair distribution function analysis. *J. Appl. Crystallogr.* **47**, 552-560 (2014).
47 Magnard, N. P. L., Anker, A. S., Aalling-Frederiksen, O., Kirsch, A. & Jensen, K. M. Ø. Characterization of intergrowth in metal oxide materials using structure-mining: the case of γ-MnO_2. *Dalton Trans.*, D2DT02153F (2022).
48 Nørskov, J. K. *et al.* Origin of the overpotential for oxygen reduction at a fuel-cell cathode. *J. Phys. Chem. B* **108**, 17886-17892 (2004).
49 García-Mota, M. *et al.* Importance of correlation in determining electrocatalytic oxygen evolution activity on cobalt oxides. *J. Phys. Chem. C* **116**, 21077-21082 (2012).
50 Bajdich, M., Garcia-Mota, M., Vojvodic, A., Nørskov, J. K. & Bell, A. T. Theoretical investigation of the activity of cobalt oxides for the electrochemical oxidation of water. *J. Am. Chem. Soc.* **135**, 13521-13530 (2013).